



SN 2022joj: A Peculiar Type Ia Supernova Possibly Driven by an Asymmetric Helium-shell Double Detonation

Chang Liu (刘畅)^{1,2}, Adam A. Miller^{1,2}, Samuel J. Boos³, Ken J. Shen⁴, Dean M. Townsley³, Steve Schulze⁵, Luke Harvey⁶, Kate Maguire⁶, Joel Johansson⁵, Thomas G. Brink⁷, Umut Burgaz⁶, Georgios Dimitriadis⁶, Alexei V. Filippenko⁷, Saarah Hall^{1,2}, K-Ryan Hinds⁸, Andrew Hoffman⁹, Viraj Karambelkar¹⁰, Charles D. Kilpatrick², Daniel Perley⁸, Neil Pichay⁷, Huei Sears^{1,2}, Jesper Sollerman¹¹, Robert Stein¹⁰, Jacco H. Terwel^{6,12}, WeiKang Zheng⁷, Matthew J. Graham¹⁰, Mansi M. Kasliwal¹⁰, Leander Lacroix^{5,13}, Josiah Purdum¹⁴, Benjamin Rusholme¹⁵, and Avery Wold¹⁵

¹ Department of Physics and Astronomy, Northwestern University, 2145 Sheridan Road, Evanston, IL 60208, USA

² Center for Interdisciplinary Exploration and Research in Astrophysics (CIERA), Northwestern University, 1800 Sherman Avenue, Evanston, IL 60201, USA

³ Department of Physics & Astronomy, University of Alabama, Tuscaloosa, AL, USA

⁴ Department of Astronomy and Theoretical Astrophysics Center, University of California, Berkeley, CA 94720-3411, USA

⁵ The Oskar Klein Centre, Department of Physics, Stockholm University, Albanova University Center, SE-106 91 Stockholm, Sweden

⁶ School of Physics, Trinity College Dublin, The University of Dublin, Dublin 2, Ireland

⁷ Department of Astronomy, University of California, Berkeley, CA 94720-3411, USA

⁸ Astrophysics Research Institute, Liverpool John Moores University, Liverpool Science Park, 146 Brownlow Hill, Liverpool L3 5RF, UK

⁹ Institute for Astronomy, University of Hawai'i at Manoa, 2680 Woodlawn Drive, Honolulu, HI 96822, USA

¹⁰ Division of Physics, Mathematics and Astronomy, California Institute of Technology, Pasadena, CA 91125, USA

¹¹ The Oskar Klein Center, Department of Astronomy, Stockholm University, Albanova University Center, SE-106 91 Stockholm, Sweden

¹² Isaac Newton Group (ING), Apt. de correos 321, E-38700, Santa Cruz de La Palma, Canary Islands, Spain

¹³ LPNHE, CNRS/IN2P3, Sorbonne Université, Université Paris-Cité, Laboratoire de Physique Nucléaire et de Hautes Énergies, 75005 Paris, France

¹⁴ Caltech Optical Observatories, California Institute of Technology, Pasadena, CA 91125, USA

¹⁵ IPAC, California Institute of Technology, 1200 E. California Boulevard, Pasadena, CA 91125, USA

Received 2023 July 31; revised 2023 September 22; accepted 2023 September 29; published 2023 November 24

Abstract

We present observations of SN 2022joj, a peculiar Type Ia supernova discovered by the Zwicky Transient Facility. SN 2022joj exhibits an unusually red $g_{\text{ZTF}} - r_{\text{ZTF}}$ color at early times and a rapid blueward evolution afterward. Around maximum brightness, SN 2022joj shows a high luminosity ($M_{g_{\text{ZTF}}, \text{max}} \simeq -19.7$ mag), a blue broadband color ($g_{\text{ZTF}} - r_{\text{ZTF}} \simeq -0.2$ mag), and shallow Si II absorption lines, consistent with those of overluminous, SN 1991T-like events. The maximum-light spectrum also shows prominent absorption around 4200 Å, which resembles the Ti II features in subluminous, SN 1991bg-like events. Despite the blue optical-band colors, SN 2022joj exhibits extremely red ultraviolet minus optical colors at maximum luminosity ($u - v \simeq 0.6$ mag and $uvw1 - v \simeq 2.5$ mag), suggesting a suppression of flux at $\sim 2500\text{--}4000$ Å. Strong C II lines are also detected at peak. We show that these unusual spectroscopic properties are broadly consistent with the helium-shell double detonation of a sub-Chandrasekhar mass ($M \simeq 1 M_{\odot}$) carbon/oxygen white dwarf from a relatively massive helium shell ($M_s \simeq 0.04\text{--}0.1 M_{\odot}$), if observed along a line of sight roughly opposite to where the shell initially detonates. None of the existing models could quantitatively explain all the peculiarities observed in SN 2022joj. The low flux ratio of [Ni II] $\lambda 7378$ to [Fe II] $\lambda 7155$ emission in the late-time nebular spectra indicates a low yield of stable Ni isotopes, favoring a sub-Chandrasekhar mass progenitor. The significant blueshift measured in the [Fe II] $\lambda 7155$ line is also consistent with an asymmetric chemical distribution in the ejecta, as is predicted in double-detonation models.

Unified Astronomy Thesaurus concepts: Supernovae (1668); Type Ia supernovae (1728); White dwarf stars (1799); Observational astronomy (1145); Surveys (1671)

Supporting material: machine-readable table

1. Introduction

Type Ia supernovae (SNe Ia) come from thermonuclear explosions of carbon/oxygen (C/O) white dwarfs (WDs) in binary systems. While there is broad consensus about this fact, specifics about the binary companion and the conditions that spark ignition remain uncertain (e.g., Maoz et al. 2014; Liu et al. 2023b, for reviews). Multiple explosion channels have

been proposed, though none of them can fully explain the diversity in the SN Ia population.

Recent attention has been focused on the helium-shell double-detonation scenario as a potential explanation for some normal SNe Ia (e.g., Polin et al. 2019; Shen et al. 2021b) as well as for a growing subclass of peculiar, red SNe Ia (e.g., Jiang et al. 2017; De et al. 2019; Liu et al. 2023a). In a double detonation, a detonation moving along the base of a helium shell (accreted from a helium-rich companion) atop the primary WD sends an oblique shock wave inward (e.g., Fink et al. 2010), which eventually converges somewhere within the core, triggers a secondary detonation, and inevitably explodes the entire WD (Nomoto 1982a, 1982b; Woosley et al. 1986;



Original content from this work may be used under the terms of the [Creative Commons Attribution 4.0 licence](https://creativecommons.org/licenses/by/4.0/). Any further distribution of this work must maintain attribution to the author(s) and the title of the work, journal citation and DOI.

Livne 1990; Woosley & Weaver 1994; Livne & Arnett 1995). This mechanism can dynamically ignite WDs well below the Chandrasekhar mass (M_{Ch} ; $\sim 1.4 M_{\odot}$). It has been proposed that a substantial fraction of SNe Ia could result from double detonations based on observations of (i) the intrinsic event rate and delay time distribution of the SN Ia population (Ruiter et al. 2011, 2014); (ii) the nucleosynthetic yields of SNe Ia as measured in their late-time spectra (Maguire et al. 2018; Flörs et al. 2020); (iii) the chemical enrichment history of various galaxies (Kirby et al. 2019; de los Reyes et al. 2020; Sanders et al. 2021; Eitner et al. 2023); and (iv) hypervelocity Galactic WDs, which are likely surviving donors from double-degenerate binaries where the primary WD has exploded in a double detonation (Shen et al. 2018a; El-Badry et al. 2023).

The remarkable observational properties for SNe Ia from double detonations are mostly associated with the helium shell. Shortly after the shell detonation, the decay of the radioactive species synthesized during the helium burning may power a flux excess in the early-time light curves (Woosley & Weaver 1994; Fink et al. 2010; Kromer et al. 2010). Afterward, the iron-group elements (IGEs) in the helium-shell ashes may provide significant line blanketing blueward of $\sim 5000 \text{ \AA}$ (Kromer et al. 2010), efficiently suppressing flux in the blue optical. In general, progenitors with a thin helium shell would show minimal detectable effects from the shell detonation, and reproduce “normal” luminosity and spectroscopic properties (e.g., those of SN 2011fe; Nugent et al. 2011) around maximum luminosity (e.g., Polin et al. 2019; Townsley et al. 2019; Magee et al. 2021; Shen et al. 2021b). Normal SNe Ia with a red flux excess shortly after the explosion may be associated with this scenario (e.g., SN 2018aoz; Ni et al. 2022). Meanwhile, objects involving a more massive helium shell exhibit peculiarities, such as a strong flash at early times and an extremely red color around maximum luminosity (Polin et al. 2019). Several peculiar SNe Ia have been interpreted as double-detonation SNe, including SN 2016jhr (Jiang et al. 2017), SN 2018byg (De et al. 2019), OGLE-2013-SN-079 (Inserra et al. 2015; interpreted as either a pure helium-shell detonation or a double detonation), SN 2016hmk (De et al. 2020; Jacobson-Galán et al. 2020; but see Galbany et al. 2019 for an alternative interpretation), SN 2019ofm (De et al. 2020), SN 2016dsg (Dong et al. 2022), SN 2020jgb (Liu et al. 2023a), and SN 2019eix (Padilla Gonzalez et al. 2023a).

Multidimensional considerations are especially important for double detonations because the explosion of the C/O core is triggered off-center, and as a result, all the observables (e.g., luminosities, colors, and absorption line features) are subject to viewing-angle effects (Fink et al. 2010; Shen et al. 2021b). Asymmetries in the chemical distribution of the SN Ia ejecta have been invoked to explain SN spectropolarimetric measurements (e.g., Kasen et al. 2003; Wang et al. 2003; Patat et al. 2012; see Wang & Wheeler 2008 for a review) and the kinematics of Ni and Fe in the innermost ejecta (Motohara et al. 2006; Maeda et al. 2010a, 2010b; Maguire et al. 2018; Li et al. 2021). To accurately infer the progenitor of a double-detonation SN, one needs to compare the observations with multidimensional models.

In this paper, we present observations of a peculiar SN Ia, SN 2022joj, which shows a remarkable color evolution, starting with red optical colors that quickly evolve to blue as the SN rises to maximum luminosity. Its photometric and spectroscopic features are qualitatively consistent with those of a

double-detonation SN. In Section 2, we summarize the observations of SN 2022joj, which are analyzed in Section 3, where we show its peculiarities in various aspects. In Section 4.1, we discuss existing scenarios that can lead to a red color in the early light curves of an SN Ia, for which the helium-shell double-detonation scenario is the most reasonable explanation. We also show that multidimensional effects must be taken into account to explain the spectroscopic peculiarities. The indication of a sub- M_{Ch} progenitor and an asymmetric explosion is supported by the late-time spectra of SN 2022joj, which we describe in Section 4.2. In Section 4.3, we discuss possible origins of the carbon features in SN 2022joj at maximum brightness. We draw our conclusions in Section 5. After the submission of this paper, a separate study of SN 2022joj by Padilla Gonzalez et al. (2023b) was posted on arXiv, drawing similar broad conclusions.

Along with this paper, we have released the data utilized in this study and the software used for data analysis and visualization. They are available online at Zenodo under an open-source Creative Commons attribution license, doi:10.5281/zenodo.8331024, and at our GitHub repository, <https://github.com/slowdivePTG/SN2022joj>.

2. Observations

2.1. Discovery and Classification

SN 2022joj was discovered by the Zwicky Transient Facility (ZTF; Bellm et al. 2019b; Graham et al. 2019; Dekany et al. 2020) on 2022 May 08.298 (UTC dates are used throughout the paper; MJD 59,707.298) with the 48 inch Samuel Oschin Telescope (P48) at Palomar Observatory, via the ZOGY image-differencing algorithm (Zackay et al. 2016), which is utilized by the automated ZTF discovery pipeline (Masci et al. 2019). It was first detected with $r_{\text{ZTF}} = 19.13 \pm 0.06 \text{ mag}$ at $\alpha_{\text{J2000}} = 14^{\text{h}}41^{\text{m}}40^{\text{s}}.08$, $\delta_{\text{J2000}} = +03^{\circ}00'24''14$ and announced to the public by Fremling (2022). A real-time alert (Patterson et al. 2019) was generated as the candidate passed internal machine-learning thresholds (e.g., Duev et al. 2019; Mahabal et al. 2019), and the internal designation ZTF22aajjjf was assigned. Follow-up observations of the SN were coordinated using the Fritz marshal (van der Walt et al. 2019; Coughlin et al. 2023). The last 3σ nondetection limited the brightness to $r_{\text{ZTF}} > 21.48 \text{ mag}$ on 2022 May 03.27 (MJD 59,702.27; 5.03 days before the first detection) using the ZTF forced photometry from the ZTF Forced Photometry Service (ZFPS; Masci et al. 2023). The ZTF light curves are displayed in Figure 1. SN 2022joj was also independently monitored by the Asteroid Terrestrial-impact Last Alert System (ATLAS; Tonry et al. 2018; Smith et al. 2020). With the forced photometry obtained from the ATLAS forced-photometry server (Shingles et al. 2021),¹⁶ we identified the last 3σ nondetection with ATLAS on 2022 May 04.26, 0.99 days after the last nondetection in r_{ZTF} , and put a limit of the brightness in the orange filter of $o > 19.84 \text{ mag}$.

The first spectrum was obtained on 2022 May 11.288 by Newsome et al. (2022), who found a best fit to a young Type I SN at redshift $z = 0.03$ using the Supernova Identification (SNID) algorithm (Blondin & Tonry 2007). In this early-time spectrum, prominent Si II $\lambda 6355$ and Ca II infrared triplet (IRT) absorption suggests an SN Ia classification, but the

¹⁶ <https://fallingstar-data.com/forcedphot/>

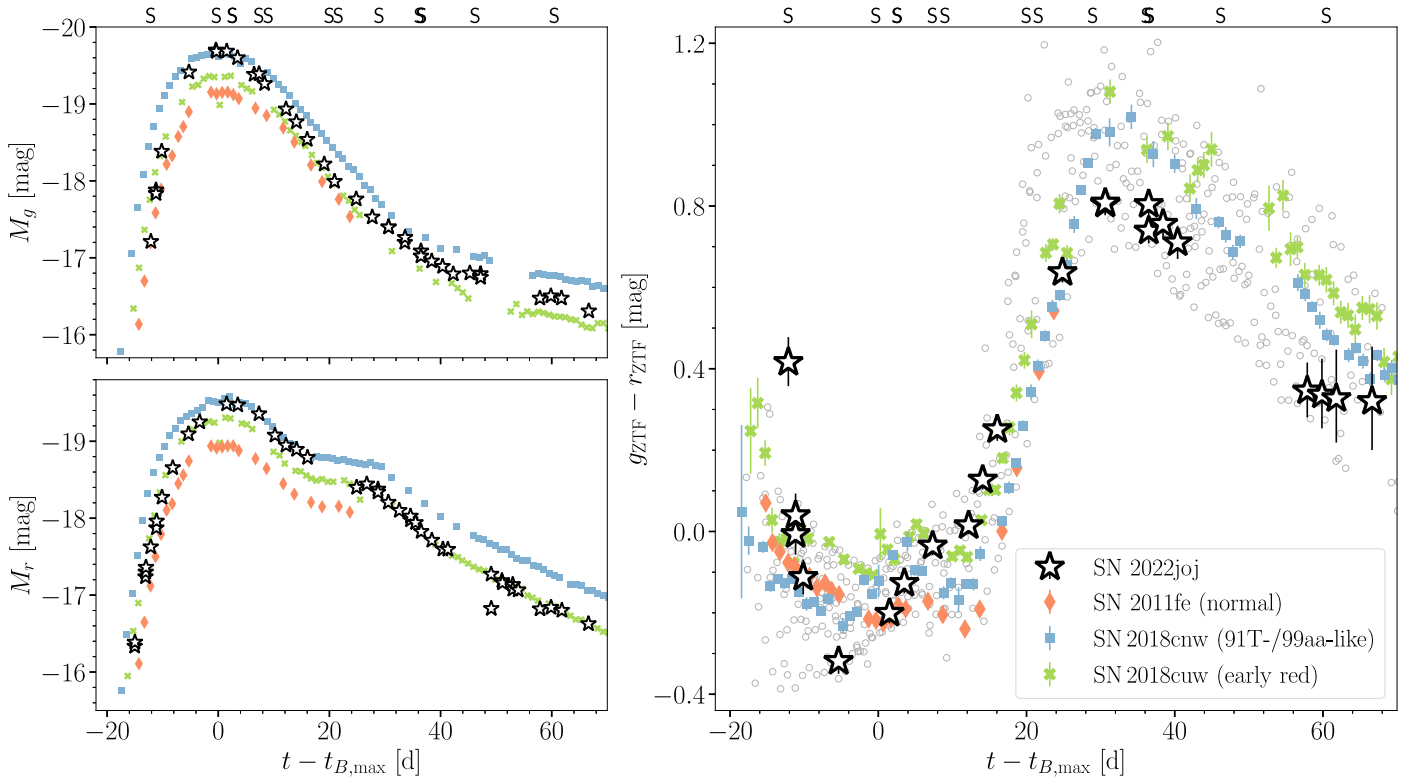


Figure 1. SN 2022joj (black stars) is an overluminous, fast-evolving SN Ia with a unique color evolution. In comparison, we show the photometric properties of SN 2011fe (normal SN Ia; Pereira et al. 2013), SN 2018cnw (91T/99aa-like), and SN 2018cuw (normal SN Ia with a red early color). Left: multiband light curves. The upper (lower) panel shows the evolution in the g -band (r -band) absolute magnitude. Right: $g_{\text{ZTF}} - r_{\text{ZTF}}$ color evolution. The gray circles denote the color evolution of 14 nearby ($z \leq 0.05$) SNe Ia (open circles) from the ZTF sample with prompt observations within 5 days of first light (Bulla et al. 2020). The phases with respect to $t_{B,\text{max}}$ (MJD 59,722.77) are measured in the rest frame of the host galaxy. Correction for Galactic extinction has been applied, but K -corrections have not been performed. The epochs of optical spectroscopy are marked with “S” on the top axis.

overall spectral shape, featuring a relatively red continuum (see Figure 2), is atypical for a normal SN Ia at this phase. Chu et al. (2022) used a peak-luminosity spectrum to indisputably classify SN 2022joj as an SN Ia based on its blue color and persistent Si II features.

2.2. Host Galaxy

The host of SN 2022joj is a dwarf galaxy at $\alpha_{J2000} = 14^{\text{h}}41^{\text{m}}40^{\text{s}}.04$, $\delta_{J2000} = +03^{\circ}00'24''.53$, as cataloged in the DESI Legacy Imaging Survey (LS; Dey et al. 2019), which reports 3σ detections in grz and W_1 (see Table 1). SN 2022joj has a projected offset of only $0''.5 \pm 0''.1$ from the host (corresponding to a projected distance of 0.27 ± 0.05 kpc at the redshift estimated below).

In addition, the SN field was observed in *grizy* as part of the wide survey of the Hyper Suprime-Cam Subaru Strategic Program (HSC-SSP; Aihara et al. 2018). We retrieved the stacked science-ready images from the HSC-SSP data archive using the HSC data access tools.¹⁷ The photometry was extracted with the aperture photometry tool presented by Schulze et al. (2018). The measurements were calibrated against a set of stars from the Pan-STARRS catalog (Chambers et al. 2016), and we applied color terms from the HSC pipeline version 8¹⁸ to correct for differences between the Pan-STARRS and HSC filters. Table 1 summarizes all measurements.

To determine the redshift of the host, we obtained two spectra about 300 days after the SN maximum brightness. On 2023 March 14, we took a spectrum of both the SN and the host using Binospec (Fabricant et al. 2019) on the 6.5 m MMT telescope with a total integration time of 5400 s. We placed the slit across both the center of the galaxy and the position of the SN (Figure 3). On 2023 April 26, we took another spectrum using the Low Resolution Imaging Spectrometer (LRIS; Oke et al. 1995) on the Keck I 10 m telescope. The slit was placed at the same position angle, with the Cassegrain Atmospheric Dispersion Compensator (Phillips et al. 2006) module on. The total integration time was 3600 s. The LRIS spectrum has a higher signal-to-noise ratio (S/N), in which we detected a potential host emission line at 6742.4 \AA (see Figure 3) with an S/N¹⁹ of 3.4. We associated this feature with H α emission, meaning the corresponding redshift of the host galaxy is $z = 0.02736 \pm 0.0007$, in agreement with the initial estimate, $z = 0.03$, from matching the SN spectra to SNID templates (Newsome et al. 2022). In the coadded 2D spectrum, the trace is dominated by the light of the SN in the nebular phase, while the center of this emission feature has an offset of $\sim 3\text{--}4$ pixels from the center of the trace. The CCDs on LRIS have a scale of $0''.135 \text{ pixel}^{-1}$, so this offset corresponds to an angular offset of $\sim 0''.4\text{--}0''.5$, consistent with the astrometric offset when comparing the LS detection of the host and the ZTF detection of the SN. The Binospec spectrum has a lower S/N, and we cannot identify this emission line at the same position in the 2D

¹⁷ <https://hsc-gitlab.mtk.nao.ac.jp/ssp-software/data-access-tools>

¹⁸ https://hsc.mtk.nao.ac.jp/pipedoc/pipedoc_8_e/colorterm.html

¹⁹ We fit the emission line with a Gaussian profile to estimate its intensity, and the S/N is defined as the intensity divided by its uncertainty.

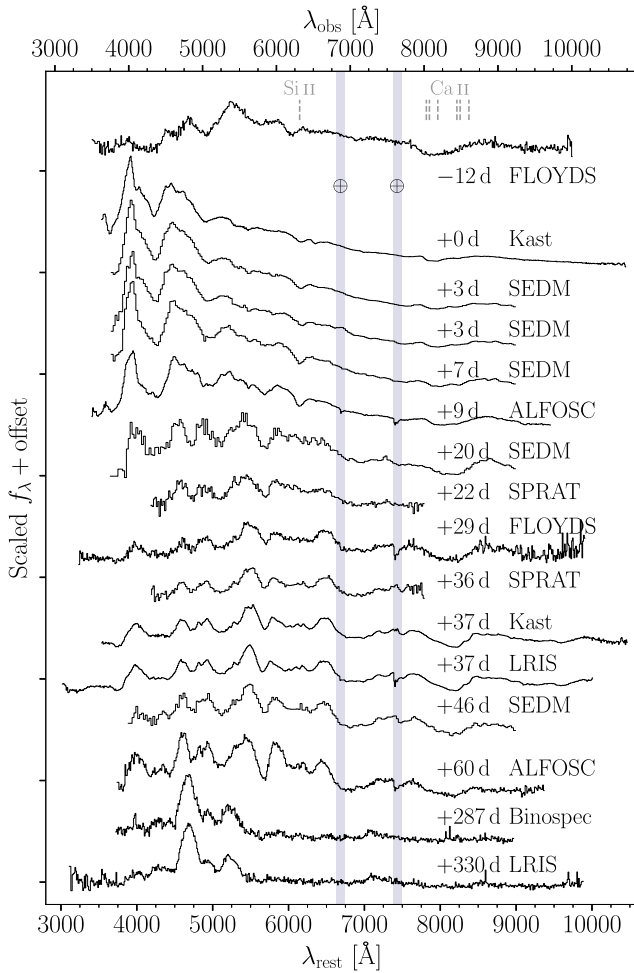


Figure 2. Optical spectral sequence of SN 2022joj showing the red to blue color transition as the SN rises to its maximum luminosity and the development of prominent absorption features around 4200 Å post-maximum. The rest-frame phase relative to the *B*-band peak and the instrument used to observe the SN are listed for each spectrum. Spectra have been corrected for $E(B - V)_{\text{MW}} = 0.032$ mag. All spectra are binned with a bin size of 10 Å, except for the low-resolution SEDM spectra. The corresponding wavelengths of the Si II $\lambda 6355$ line (with an expansion velocity of $10,000 \text{ km s}^{-1}$) and the Ca II IRT (with expansion velocities of both $10,000 \text{ km s}^{-1}$ and $25,000 \text{ km s}^{-1}$) are marked by the vertical dashed lines. The strong optical telluric features (Fraunhofer *A* and *B* bands) are marked by the shaded regions.

Table 1
Host Photometry of SN 2022joj

Survey	Filter	m (mag)	σ_m (mag)
HSC-SSP	PS <i>g</i>	22.01	0.03
HSC-SSP	PS <i>r</i>	21.63	0.02
HSC-SSP	PS <i>i</i>	21.54	0.03
HSC-SSP	PS <i>z</i>	21.37	0.04
HSC-SSP	PS <i>y</i>	21.22	0.09
LS	DECam <i>g</i>	22.05	0.05
LS	DECam <i>r</i>	21.65	0.05
LS	DECam <i>z</i>	21.39	0.10
LS	W_1	21.94	0.35

Notes. HSC-SSP—Hyper Suprime-Cam Subaru Strategic Program; LS—DESI Legacy Imaging Survey; PS—Pan-STARRS; DECam—Dark Energy Camera. All magnitudes are reported in the AB system (Oke & Gunn 1983) and are not corrected for reddening.

spectrum via visual inspection. Nevertheless, we marginally detect an emission feature in the 1D spectrum with an S/N of 1.5 at the same wavelength. All the evidence indicates that the H α detection is real.

We estimated the distance modulus of SN 2022joj in the following way. We first used the 2M++ model (Carrick et al. 2015) to estimate the peculiar velocity of the host galaxy, which turned out to be $244 \pm 250 \text{ km s}^{-1}$. Then the peculiar velocity was combined with the recession velocity in the frame of the cosmic microwave background $v_{\text{CMB}} = 8424 \text{ km s}^{-1}$, which yielded a net Hubble recession rate of $8193 \pm 250 \text{ km s}^{-1}$. Using cosmological parameters $H_0 = 70 \text{ km s}^{-1} \text{ Mpc}^{-1}$, $\Omega_M = 0.3$, and $\Omega_\Lambda = 0.7$, the estimated luminosity distance to SN 2022joj was 119.5 Mpc, equivalent to a distance modulus of 35.39 ± 0.03 mag.

2.3. Optical Photometry

SN 2022joj was monitored in ZTF's *gri* bands as part of its ongoing Northern Sky Survey (Bellm et al. 2019a). The i_{ZTF} data do not cover the rise. We used the forced-photometry light curves from ZFPS, reduced using the pipeline from A. A. Miller et al. (2023, in preparation); see also Yao et al. (2019). We adopted a Galactic extinction of $E(B - V)_{\text{MW}} = 0.032$ mag (Schlafly & Finkbeiner 2011), and corrected all photometry using the extinction model from Fitzpatrick (1999) assuming $R_V = 3.1$. We did not find any Na I D absorption at the redshift of the host galaxy (we put a 3σ upper limit in the equivalent width of Na I D₁ + D₂ of $<0.5 \text{ Å}$), indicating that the extinction from the host is negligible. The blue $g_{\text{ZTF}} - r_{\text{ZTF}}$ color (~ -0.2 mag) near the maximum luminosity after correcting for Galactic extinction is also consistent with no additional reddening from the host. Therefore we assumed $E(B - V)_{\text{host}} = 0$. The dereddened g_{ZTF} and r_{ZTF} forced-photometry light curves in absolute magnitudes are shown in Figure 1. Additional observations of SN 2022joj were obtained in the *o* and *c* filters in the ATLAS survey, in the *griz* filters with the optical imaging component of the infrared–Optical suite of instruments (IO:O) on the Liverpool Telescope (LT), in the *griBVRI* filters and the clear filter on the 0.76 m Katzman Automatic Imaging Telescope (KAIT; Filippenko et al. 2001) at Lick Observatory, and in the *BVRI* filters on the 1 m Anna Nickel telescope at Lick. The ZTF, ATLAS, LT, KAIT, and Nickel observations are reported in Table 2. The ZTF *gri* magnitudes, ATLAS *o* and *c* magnitudes, and Sloan *griz* magnitudes are reported in the AB system, while the *BVRI* and clear magnitudes are reported in the Vega system.

2.4. Swift Ultraviolet/Optical Telescope Observations

UV observations of SN 2022joj were obtained using the Ultraviolet/Optical Telescope (UVOT; Roming et al. 2005) on the Neil Gehrels Swift Observatory (Swift; Gehrels et al. 2004) following a target-of-opportunity request by E. Padilla Gonzalez. Prior to the SN, UVOT images of the field had been obtained in the *u*, *uvw1*, and *uvw2* filters. In each of these reference images the flux at the location of the SN is consistent with 0, and the 3σ upper limits correspond to $\lesssim 10\%$ of the SN flux measured in the UV. In the optical bands, the LS photometry ($g = 22.05 \pm 0.05$ mag) shows that the host galaxy contributes $\lesssim 1\%$ of the total observed flux. We therefore concluded that the host galaxy can be neglected when estimating the SN flux in UVOT images.

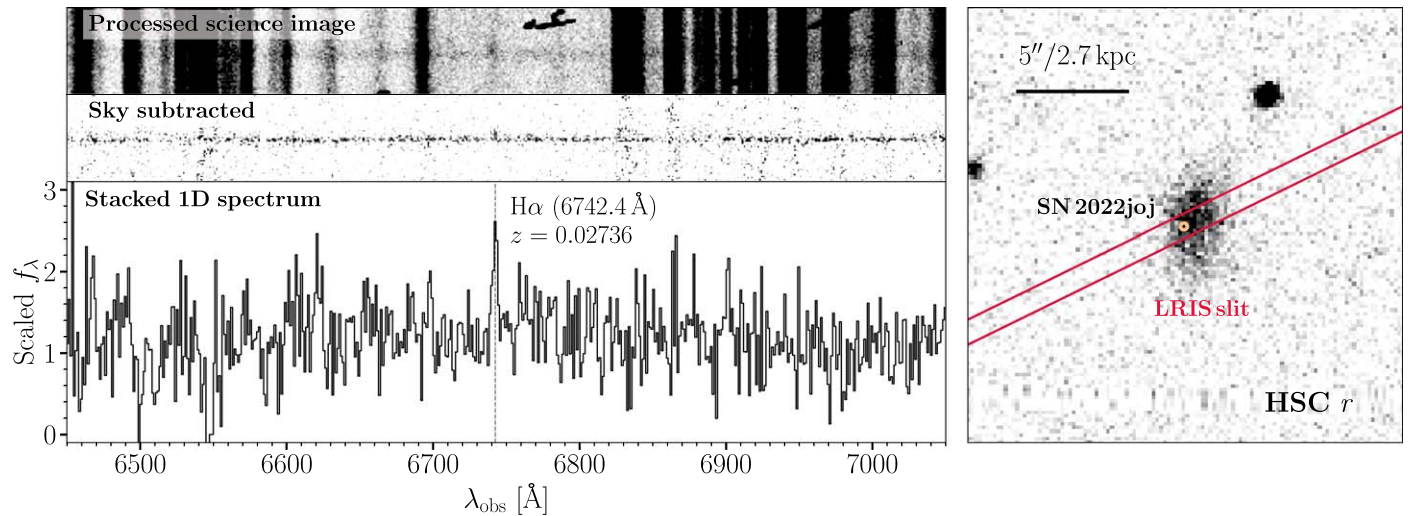


Figure 3. The LRIS spectrum reveals an $\text{H}\alpha$ emission line from the host galaxy at 6742.4 \AA , corresponding to $z = 0.02736$. Left: the $\text{H}\alpha$ emission in the observed 2D and 1D spectra. This emission line sits in a region free of strong night-sky lines and is unlikely to be due to bad sky subtraction. Right: image of the host galaxy and the position of SN 2022joj, with the orientation of the LRIS slit overlotted.

Table 2
Optical and UV Photometry of SN 2022joj

t_{obs} (MJD)	Filter	m (mag)	σ_m (mag)	Magnitude System	Telescope
59,707.298	ZTF r	19.131	0.064	AB	P48/ZTF
59,707.340	ZTF r	19.078	0.043	AB	P48/ZTF
59,709.295	ZTF r	18.229	0.037	AB	P48/ZTF
59,709.342	ZTF r	18.167	0.030	AB	P48/ZTF
59,709.381	ZTF r	18.105	0.023	AB	P48/ZTF

Notes. Observed magnitudes in the ZTF, ATLAS, UVOT, LT, KAIT, and Nickel passbands. Correction for Galactic extinction has not been applied.

(This table is available in its entirety in machine-readable form.)

We determined the flux in the u , b , v , $uvw1$, $uvm2$, and $uvw2$ filters using a circular aperture with a radius of $5''$ centered at the position of the SN. To estimate the brightness of the sky background we used a coaxial annulus region with an inner/outer radius of $8''/15''$. Reduction was performed with the pipeline `Swift_ToO`²⁰ based on the package `HEASOFT`²¹ version 6.30.1 (HEASARC 2014). The magnitudes are also reported in Table 2 in the Vega system.

2.5. Optical Spectroscopy

We obtained a series of optical spectra of SN 2022joj using the Spectral Energy Distribution Machine (SEDm; Blagorodnova et al. 2018) on the automated 60 inch telescope (P60; Cenko et al. 2006) at Palomar Observatory, the Kast double spectrograph (Miller & Stone 1994) on the Shane 3 m telescope at Lick Observatory, the Andalucia Faint Object Spectrograph and Camera (ALFOSC)²² installed at the 2.56 m Nordic Optical Telescope (NOT), the Spectrograph for the Rapid Acquisition of Transients (SPRAT; Piascik et al. 2014) on the 2 m LT (Steele et al. 2004) under program PL22A13

(PI: Dimitriadis), the FLOYDS spectrograph²³ on the 2 m Faulkes Telescope South (FTS) at Siding Spring as part of the Las Cumbres Observatory (Brown et al. 2013), Binospec on the 6.5 m MMT telescope, and LRIS on the Keck I 10 m telescope. The SEDM spectra were reduced using the custom `pysemdm` software package (Rigault et al. 2019). The Shane/Kast spectra, obtained with the slit near the parallactic angle to minimize differential slit losses (Filippenko 1982), were reduced following the standard techniques for CCD processing and spectrum extraction (Silverman et al. 2012) utilizing IRAF (Tody 1986) routines and custom Python and IDL codes.²⁴ The NOT/ALFOSC, Keck I/LRIS, and MMT/Binospec spectra were reduced using the `PyPeIt` package (Prochaska et al. 2020). The LT/SPRAT spectra were reduced with a dedicated pipeline²⁵ for bias subtraction, flat-fielding, derivation of the wavelength solution, and flux calibration, with additional IRAF/`PyRAF`²⁶ routines for proper extraction of the spectra. The FTS/FLOYDS spectrum was reduced using the FLOYDS pipeline.²⁷ We also attempted to obtain a near-infrared spectrum with the Triple Spectrograph (TSPEC)²⁸ installed at the 200 inch Hale telescope (P200; Oke & Gunn 1982) at Palomar Observatory, but the observations were mostly characterized by low S/N and a few broad undulations with no immediately identifiable lines. Thus, the TSPEC data were excluded from our analysis. Details of the spectroscopic observations are listed in Table 3. The resulting spectral sequence is shown in Figure 2. All of the spectra listed in Table 3 will be available on WISEREP (Yaron & Gal-Yam 2012).

We also included the spectrum uploaded to the Transient Name Server (TNS) by Newsome et al. (2022) in our analysis,

²³ <https://lco.global/observatory/instruments/floyds/>

²⁴ <https://github.com/ishivvers/TheKastShiv>

²⁵ https://github.com/LivTel/sprat_l2_pipeline

²⁶ IRAF is distributed by the National Optical Astronomy Observatory, which is operated by the Association of Universities for Research in Astronomy (AURA) under a cooperative agreement with the U.S. National Science Foundation (NSF).

²⁷ <https://lco.global/documentation/data/floyds-pipeline/>

²⁸ <https://sites.astro.caltech.edu/palomar/observer/200inchResources/tspecspecs.html>

²⁰ https://github.com/slowdivePTG/Swift_ToO

²¹ <http://heasarc.gsfc.nasa.gov/ftools>

²² <http://www.not.iac.es/instruments/alfosc/>

Table 3
Spectroscopic Observations of SN 2022joj

t_{obs} (MJD)	Phase (days)	Telescope/ Instrument	R ($\lambda/\Delta\lambda$)	Range (\AA)
59,710.29	−12.1	FTN/FLOYDS-N	550	3500–10000
59,722.43	−0.3	Shane/Kast	750	3630–10730
59,725.34	+2.6	P60/SEDm	100	3770–9220
59,725.43	+2.6	P60/SEDm	100	3770–9220
59,730.27	+7.4	P60/SEDm	100	3770–9220
59,732.02	+9.0	NOT/ALFOSC	360	3500–9700
59,743.28	+20.0	P60/SEDm	100	3770–9220
59,744.24	+20.9	P200/TSpec	2500	10000–24630
59,744.96	+21.6	LT/SPRAT	350	4020–7990
59,752.50	+29.0	FTS/FLOYDS-S	550	3500–10000
59,759.92	+36.2	LT/SPRAT	350	4020–7990
59,760.28	+36.5	Shane/Kast	750	3630–10750
59,760.37	+36.7	Keck I/LRIS	1100	3100–10280
59,770.25	+46.3	P60/SEDm	100	3770–9220
59,784.89	+60.5	NOT/ALFOSC	280	3850–9620
60,017.42	+286.9	MMT/Binospec	1340	3830–9210
60,061.56	+329.8	Keck I/LRIS	1100	3200–10150

Notes. Phase is measured relative to the B -band peak in the rest frame of the host galaxy. The resolution R is reported for the central region of the spectrum.

which was obtained using the FLOYDS spectrograph on the 2 m Faulkes Telescope North (FTN) at Haleakala.

3. Analysis

3.1. Early Light Curves and the First Light

To estimate the time of first light (t_{fl}), we assume an initial power-law rise in the broadband flux $f(t)$,

$$f(t) = A(t - t_{\text{fl}})^{\alpha},$$

where A is a constant and α is the power-law index. We only include the forced-photometry light curve with flux $\leq 40\%$ of the peak luminosity (Miller et al. 2020) in r_{ZTF} and ATLAS o , in which observations were conducted on more than three nights between -20 and -10 days. Light curves in other bands are excluded because the coverage is significantly worse at this phase (see Section 3.2). We assume that t_{fl} is the same in both bands, then estimate α and A in each band with a Bayesian approach. We adopt flat priors for t_{fl} and $\log A$, and a normal prior for each α centered at 2 (the fireball model) with a standard deviation of 1. We sample their posterior distributions with Markov Chain Monte Carlo (MCMC) using the package PyMC (Salvatier et al. 2016). In addition, we run another model with a fixed $\alpha = 2$. The estimated model parameters are listed in Table 4. We find that both light curves are consistent with a power-law rise from MJD 59,703.16 $^{+0.70}_{-0.58}$. This estimate is consistent with the $\alpha = 2$ fireball model. When fixing $\alpha = 2$, the model also fits the light curve well, but the estimated t_{fl} is ~ 0.5 days later (MJD 59,703.66 $^{+0.10}_{-0.11}$). We do not find any correlated residuals as evidence for a flux excess after ~ 4 days from t_{fl} , although a flux excess before the first detection cannot be ruled out.

3.2. Photometric Properties

The basic photometric properties of SN 2022joj are listed in Table 4. The times of the maximum luminosity and the corresponding magnitudes in the ZTF gr bands and the KAIT/Nickel $BVRi$ bands are estimated using a fourth-order polynomial fit. We do not include the maximum i_{ZTF} -band properties, which are relatively uncertain owing to the low cadence in i_{ZTF} around peak.

SN 2022joj shows a few peculiar photometric features compared to normal SNe Ia. In Figure 1, we compare the g_{ZTF} and r_{ZTF} light curves and $g_{\text{ZTF}} - r_{\text{ZTF}}$ color evolution of SN 2022joj with those of the well-observed normal SN Ia SN 2011fe,²⁹ as well as those of SN 2018cnw (ZTF18abapujr) and SN 2018cuw (ZTF18abcflnz) from a sample of SNe Ia with prompt observations within 5 days of first light by ZTF (Yao et al. 2019; Bulla et al. 2020). SN 2018cnw is slightly overluminous at peak, and belongs to either the SN 1999aa-like (99aa-like; Garavini et al. 2004) or the SN 1991T-like (91T-like; Filippenko et al. 1992b) subclass of SNe Ia, while SN 2018cuw is a normal SN Ia with a red $g_{\text{ZTF}} - r_{\text{ZTF}}$ color comparable to that of SN 2022joj ~ 15 days prior to peak.

Around maximum brightness, SN 2022joj is overluminous, comparable to SN 2018cnw, and ~ 0.5 mag brighter than SN 2011fe in both g_{ZTF} and r_{ZTF} . But SN 2022joj clearly stands out owing to its fast evolution in g_{ZTF} . While SN 2022joj and SN 2018cnw show a similar maximum brightness in g_{ZTF} , upon the first detection of SN 2022joj in g_{ZTF} at ~ -12 days, its corresponding absolute magnitude (-17.2 mag) is ~ 0.8 mag fainter than that of SN 2018cnw at a similar phase. This means on average, SN 2022joj rises faster than SN 2018cnw by ~ 0.06 mag day $^{-1}$ in g_{ZTF} during that period of time. On the decline, the $\Delta m_{15}(g_{\text{ZTF}})$ of SN 2022joj is 1.03 ± 0.03 mag, which is significantly greater than that of the overluminous SN 2018cnw ($\Delta m_{15}(g_{\text{ZTF}}) = 0.77$ mag) or the normal SN 2011fe ($\Delta m_{15}(g_{\text{ZTF}}) = 0.80$ mag). The rapid decline of SN 2022joj is atypical for overluminous SNe Ia, which are usually the slowest decliners in the SN Ia population (Phillips et al. 1999; Taubenberger 2017). The rapid decline is probably due to the unusual and fast-developing absorption feature near 4200 \AA (see Section 3.3).

The color evolution of SN 2022joj does not match that of normal SNe Ia, as shown by the trail traced by SN 2022joj in the right panel of Figure 1. We overplot all the SNe from the ZTF early SN Ia sample (Bulla et al. 2020) with $z \leq 0.05$. They are corrected for Galactic extinction, but K -corrections have not been performed for consistency. Given the peculiar nature of SN 2022joj, we cannot use models trained on normal SNe Ia to reliably estimate its K -correction. Nevertheless, given its relatively low redshift ($z \lesssim 0.03$), the K -corrections are not expected to be large ($K(g_{\text{ZTF}} - r_{\text{ZTF}}) \simeq -0.05$ mag around maximum, estimated using the Kast spectrum at -0.3 days). For the same reason we only include the SNe Ia with the lowest redshift from the sample of Bulla et al. (2020). SN 2022joj is remarkably red ($g_{\text{ZTF}} - r_{\text{ZTF}} \simeq 0.4$ mag) at ~ -12 days (~ 7 days after t_{fl}), and is clearly an outlier compared to the normal SN Ia sample.³⁰ During the ensuing week, SN 2022joj

²⁹ We show the synthetic photometry in g_{ZTF} and r_{ZTF} calculated using the spectrophotometric sequence from Pereira et al. (2013).

³⁰ There is one point close to the first detection of SN 2022joj in the color evolution diagram, which belongs to SN 2018dhw (ZTF18abfhrnc). This single $g_{\text{ZTF}} - r_{\text{ZTF}}$ measurement has an uncertainty of ~ 0.1 mag and is 2σ redder than measurements made the nights before and after.

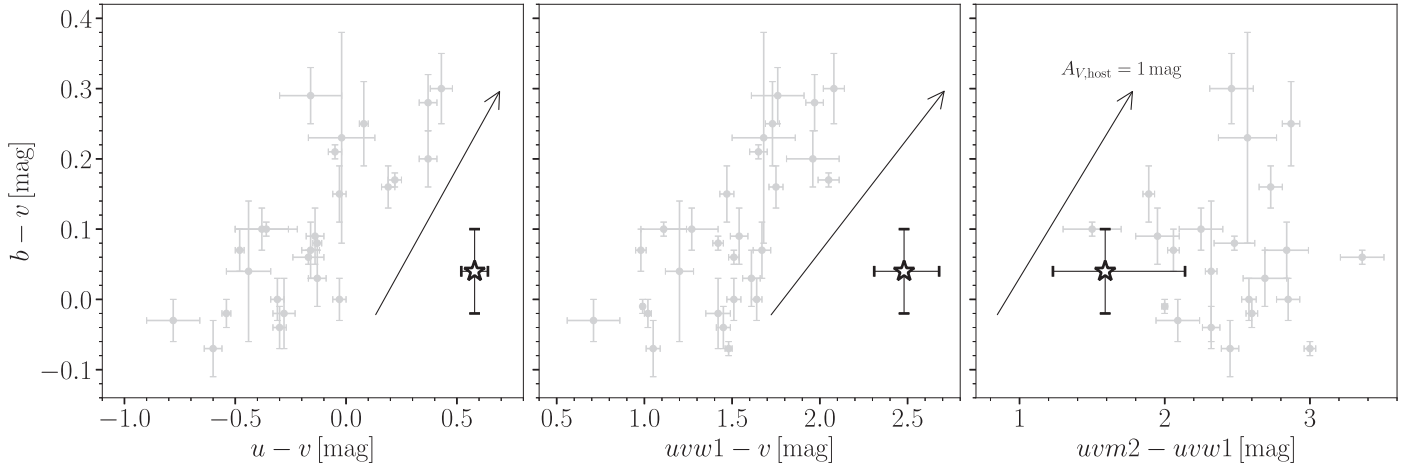


Figure 4. The color-color diagrams using UVOT photometry show that SN 2022joj (black star) has very unusual UV–optical colors at maximum luminosity compared to normal SNe Ia (gray dots; a sample of 29 normal SNe Ia from Brown et al. 2018). The arrows mark how SN 2022joj would move in each color-color space if there were host reddening with a visual extinction of $A_{V,\text{host}} = 1$ (assuming $R_V = 3.1$).

Table 4
Basic Photometric Properties of SN 2022joj

Rise (Flux $\leq 40\%$ of Peak Luminosity)						
Variable α : Prior $N(2, 1)$			Fixed α : $\alpha = 2$			
t_{fl} (MJD)	$\alpha_{\text{ZTF},r}$	$\alpha_{\text{ATLAS},o}$	$t_{\text{fl},\alpha=2}$ (MJD)			
59, 703.16 $^{+0.70}_{-0.58}$	2.18 $^{+0.20}_{-0.24}$	2.37 $^{+0.48}_{-0.20}$	59, 703.66 $^{+0.10}_{-0.11}$			
Maximum Luminosity						
Filters	g_{ZTF}	r_{ZTF}	B	V	R	I
$t_{\text{max,poly}}$ (MJD)	59,722.66 \pm 0.21	59,725.54 \pm 0.09	59,722.77 \pm 0.30	59,724.88 \pm 0.28	59,724.61 \pm 0.28	59,720.73 \pm 0.27
$M_{\text{max,poly}}$ (mag)	-19.693 \pm 0.014	-19.492 \pm 0.004	-19.456 \pm 0.011	-19.544 \pm 0.009	-19.496 \pm 0.009	-19.222 \pm 0.011

Notes. Parameters are defined in the text. The absolute magnitudes have been corrected for Galactic extinction. The uncertainty in the distance modulus (0.03 mag) and the systematics in the polynomial models are not included.

quickly evolves to the blue, and is among the bluest objects in the sample at ~ -5 days (~ 14 days after t_{R} ; $g_{\text{ZTF}} - r_{\text{ZTF}} \simeq -0.3$ mag). SN 2018cuw has a comparable $g_{\text{ZTF}} - r_{\text{ZTF}}$ color at early times, but the blueward evolution of SN 2018cuw is slower than that of SN 2022joj. No later than SN 2022joj reaches its peak luminosity, it starts to evolve redward. While other SNe Ia show qualitatively similar redward evolution, this usually happens much later ($\sim +10$ days). When $g_{\text{ZTF}} - r_{\text{ZTF}}$ reaches its maximum (~ 0.8 mag) at $\sim +30$ days, SN 2022joj is again bluer than most of the SNe Ia in the ZTF sample. Eventually as SN 2022joj steps into the transitional phase, its color evolution follows the Lira law³¹ (Lira 1996; Phillips et al. 1999) and shows no significant difference from that of the SNe Ia in the ZTF sample. The $B - V$ color evolves in a similar way to the $g_{\text{ZTF}} - r_{\text{ZTF}}$ color, which starts red ($B - V \simeq 1.2$ mag at -12 days) and quickly turns bluer, reaching $B - V \simeq 0.0$ mag at ~ -5 days before turning red again.

While SN 2022joj shows a blue $g_{\text{ZTF}} - r_{\text{ZTF}}$ color near maximum brightness, its UV – optical colors are unusually red. In Figure 4, we show the locations of SN 2022joj in the UVOT color-color diagrams compared to those of 29 normal SNe Ia with UV observations around maximum from Brown et al.

(2018). SN 2022joj stands out due to the red $u - v$ and $uvw1 - v$ colors. After correcting for Galactic extinction, SN 2022joj shows $u - v = 0.58^{+0.06}_{-0.06}$ mag and $uvw1 - v = 2.48^{+0.23}_{-0.19}$ mag. As a comparison, none of the objects in the normal SN Ia sample has $u - v > 0.5$ mag or $uvw1 - v > 2.1$ mag. This cannot be a result of the unknown host reddening, since the amount of host extinction needed to account for the red near-UV colors of SN 2022joj would require the intrinsic $b - v$ color of the SN to be unphysically blue (shifted along the opposite direction of the arrows in Figure 4). Interestingly, SN 2022joj exhibits a moderately blue mid-UV color ($uvm2 - uvw1 = 1.59^{+0.55}_{-0.36}$ mag), while most of the normal SNe Ia in the sample from Brown et al. (2018) show $uvm2 - uvw1 \gtrsim 2$ mag. This might indicate that, for some reason, the flux in the near-UV (~ 2500 – 4000 Å) of SN 2022joj is suppressed near maximum brightness.

To conclude, despite a similar luminosity and color to 99aa-like/91T-like events at maximum brightness, the rapid photometric rise and decline and the unusual color evolution of SN 2022joj both indicate that it exhibits some peculiarities relative to normal and 99aa-like/91T-like SNe Ia.

3.3. Optical Spectral Properties

In Figure 2, we show the optical spectral sequence of SN 2022joj. The -12 days spectrum exhibits prominent

³¹ The original Lira law was discovered in the $B - V$ color, but in the $g_{\text{ZTF}} - r_{\text{ZTF}}$ color we see a similar trend.

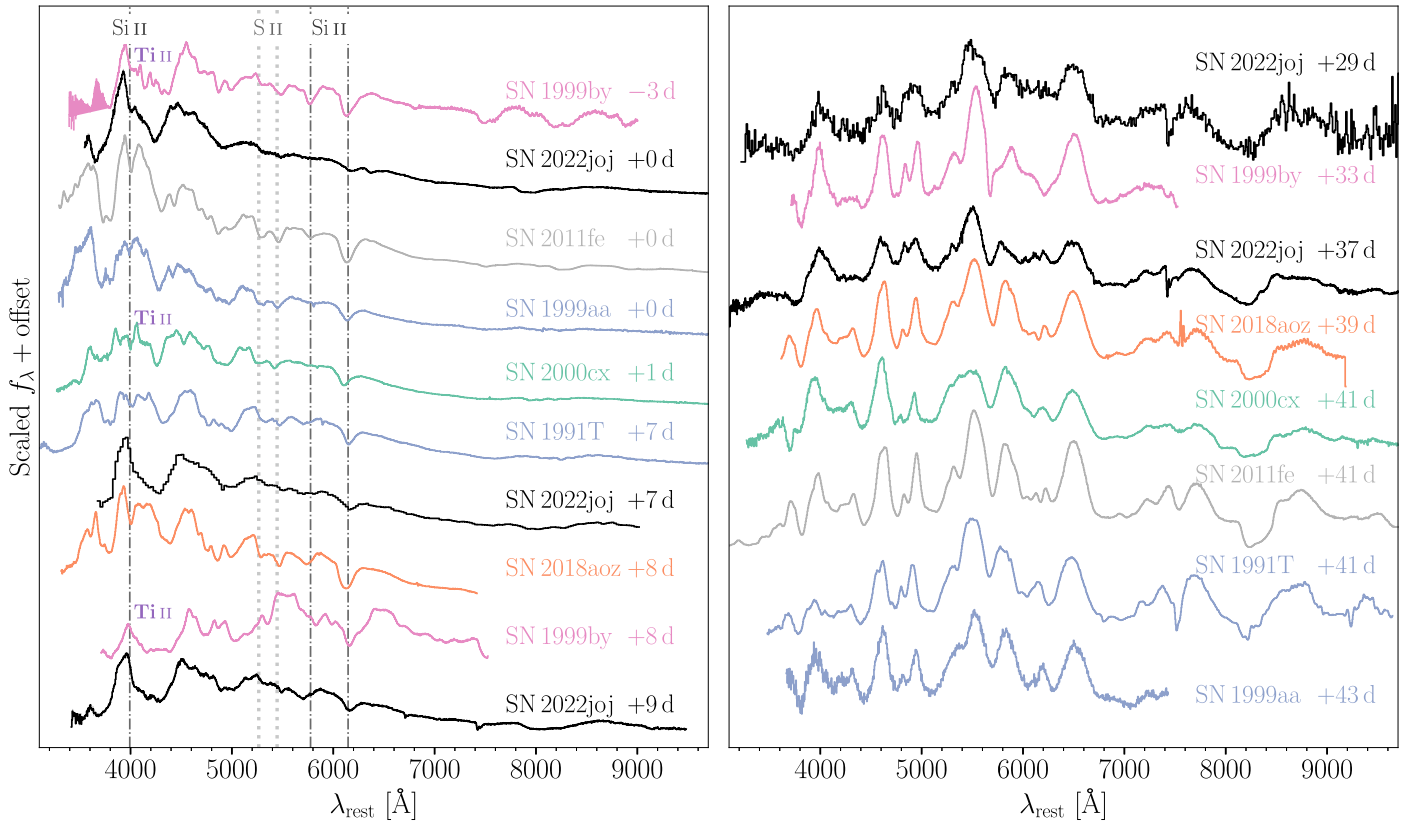


Figure 5. Optical spectra of SN 2022joj (black) and (i) a subluminal SN Ia, SN 1999by (magenta), (ii) a normal SN Ia, SN 2011fe (gray), (iii) two overluminous SNe Ia, SN 1991T and SN 1999aa (blue), (iv) the peculiar SN 2000cx (green), and (v) a normal SN Ia with a red color at early times, SN 2018aoz (orange), near maximum brightness (left panel) and about a month after maximum (right panel). The dashed–dotted lines correspond to the wavelengths of three Si II lines (4128 Å, 5972 Å, and 6355 Å), while the dotted lines correspond to the wavelengths of the S II “W-trough” (both assuming an expansion velocity of 10,000 km s^{−1}). Ti II has been identified from the spectra of SN 1999by and SN 2000cx at around 4200 Å, and the corresponding features are labeled. The spectra were downloaded from WiseREP (Yaron & Gal-Yam 2012), with the following original data sources: SN 2011fe—Pereira et al. (2013), Mazzali et al. (2014); SN 1991T, SN 1999aa, and SN 2000cx—Silverman et al. (2012); SN 1999by—Matheson et al. (2008); SN 2018aoz—Ni et al. (2023).

absorption lines associated with Si II $\lambda 6355$ and Ca II IRT (this spectrum was obtained and posted on TNS by Newsome et al. 2022). It also displays a strong suppression of flux blueward of ~ 5000 Å confirming the unusually red photometric colors at early times. Near maximum brightness, the Kast spectrum and the two SEDM spectra show a very blue continuum in the range ~ 5000 – 8000 Å with shallow absorption features, indicating a high photometric temperature. The Si II $\lambda\lambda 5972$, 6355 lines, S II W-trough, and Ca II IRT are detectable but not prominent. The C II $\lambda\lambda 6580$, 7234 lines are prominent at maximum brightness (+0 days), and quickly disappear afterward (+3 days). A wide, asymmetric absorption feature appears at ~ 4000 – 4500 Å (the 4200 Å features hereafter). There is a break on the blue edge of this feature, which we associate with Si II $\lambda 4128$, often seen in other SNe Ia. The 4200 Å features become even wider and deeper in another SEDM spectrum at +7 days and in the ALFOSC spectrum at +9 days. Weeks after the maximum, in the FLOYDS spectrum (+29 days) and the LRIS spectrum (+36 days), the bottom of the 4200 Å features becomes flat, reminiscent of the Ti-trough in subluminal SN 1991bg-like (91bg-like; Filippenko et al. 1992a; Leibundgut et al. 1993) SNe. The nebular-phase spectra are dominated by [Fe II] and [Fe III] emission lines, but the [Fe II] features (e.g., the complex around 7300 Å) are weaker than in other SNe Ia (Figure 9), suggesting that the ejecta

remain highly ionized about a year after the explosion. The nebular spectra are discussed in detail in Section 4.2.

In Figure 5, we compare the maximum-light and transition-phase spectra of SN 2022joj to those seen of other SNe Ia. Around peak, the blue continuum and shallow absorption features in SN 2022joj are similar to those of overluminous objects, including SN 1991T, SN 1999aa, and SN 2000cx. The asymmetric 4200 Å features are not seen in normal (SN 2011fe) or overluminous (SN 1991T and SN 1999aa) SNe Ia, which all show another maximum at ~ 4100 Å redward of the narrow Si II $\lambda 4128$ feature. In SN 2000cx, a similar (but narrower) absorption feature is interpreted as high-velocity Ti II (Branch et al. 2004). The 4200 Å features are actually much more similar to the well-known “Ti-trough” that is ubiquitous in subluminal 91bg-like objects, e.g., SN 1999by (Arbour et al. 1999). Prior to the peak, SN 1999by also shows this asymmetric absorption at about the same wavelength, which becomes more prominent with a nearly-flat-bottom trough about a week after maximum. This absorption is caused by a blend of multiple species dominated by Ti II (Filippenko et al. 1992a; Mazzali et al. 1997). It remains prominent in the spectrum up to one month after maximum. We find similar features in the spectra of SN 2022joj at +29 and +36 days. Other normal/overluminous SNe Ia, unlike SN 2022joj, all exhibit a dip around 4500 Å. Other than the 4200 Å features, SN 2022joj is entirely dissimilar from 91bg-like objects, which

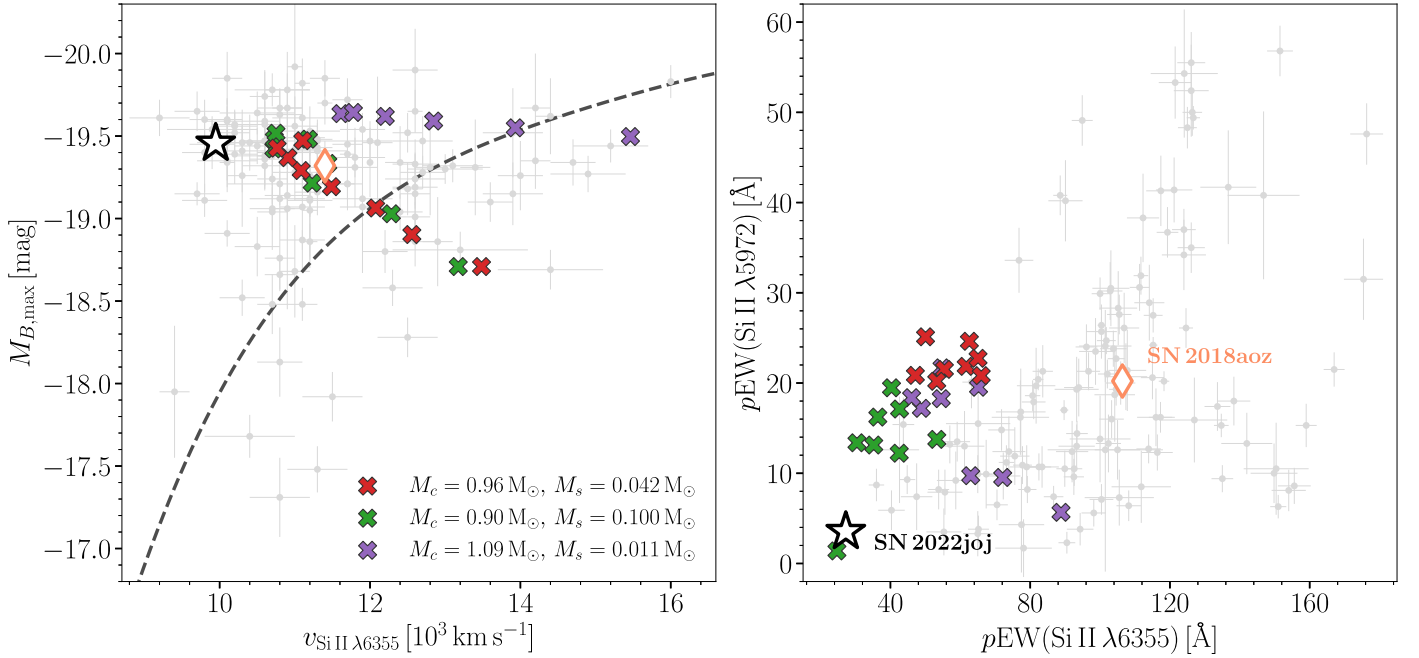


Figure 6. SN 2022joj (black star) is an SN Ia showing normal brightness in B and remarkably shallow Si II features with a relatively low expansion velocity at maximum luminosity, compared to a sample of normal SNe Ia (gray dots) from Zheng et al. (2018) and Burrow et al. (2020). Left: the B -band absolute magnitude vs. the expansion velocity of Si II $\lambda 6355$ at maximum brightness. Right: the pEWs of the two Si II lines Si II $\lambda\lambda 5972, 6355$ at maximum brightness. The dashed black line corresponds to the theoretical $M_{B,\max} - v_{\text{Si II}}$ relation of 1D double-detonation models for thin helium shells across a spectrum of progenitor masses in Polin et al. (2019). The colored \times symbols show 2D double-detonation models from Shen et al. (2021b) with different C/O core masses (M_c) and helium-shell masses (M_s), and viewing angles. For each model, multiple symbols are shown to summarize the effect of different viewing angles, from $\mu = -0.93$ to $\mu = +0.93$ (μ defined as the cosine of the polar angle relative to the point where the helium-shell detonation occurs). Parameters of the candidate double-detonation normal SN Ia SN 2018aoz (Ni et al. 2023) are also overplotted as an orange diamond.

Table 5
Fits to the Expansion Velocities and pEWs of Si II $\lambda\lambda 5972, 6355$ and the Ca II IRT of SN 2022joj

Phase (days)	Si II $\lambda 5972$		Si II $\lambda 6355$		Ca II IRT, PVFs		Ca II IRT, HVFs	
	v (10^3 km s^{-1})	pEW (\AA)	v (10^3 km s^{-1})	pEW (\AA)	v (10^3 km s^{-1})	pEW (\AA)	v (10^3 km s^{-1})	pEW (\AA)
−12.1	-15.66 ± 0.13	47.5 ± 2.5	-14.85 ± 0.83	190 ± 34	-25.98 ± 0.56	278 ± 40
−0.3	-10.10 ± 0.88	3.5 ± 1.9	-9.95 ± 0.07	27.2 ± 0.8	-12.45 ± 0.17	58 ± 2	-23.35 ± 0.06	117 ± 2
+2.5	-8.77 ± 0.63	2.9 ± 1.5	-10.28 ± 0.13	27.8 ± 1.3	-12.03 ± 0.73	58 ± 11	-22.51 ± 0.33	109 ± 11
+2.6	-8.35 ± 0.62	4.4 ± 2.6	-9.87 ± 0.28	25.4 ± 2.7	-11.77 ± 0.93	85 ± 17	-22.17 ± 0.47	105 ± 15
+7.3	-10.52 ± 0.17	40.9 ± 2.7	-10.10 ± 0.82	79 ± 18	-20.88 ± 0.57	172 ± 24
+9.0	-10.37 ± 0.04	48.5 ± 0.6	-11.94 ± 0.23	144 ± 6	-21.13 ± 0.15	127 ± 6

are $\gtrsim 2$ mag fainter at peak and exhibit much stronger Si II, Ca II, and O I absorption from a cooler line-forming region (Filippenko et al. 1992a). The Ti-trough in 91bg-like SNe is interpreted as a result of low photospheric temperature (Mazzali et al. 1997).

SN 2022joj also shows remarkably shallow Si II absorption at maximum brightness. Following the techniques elaborated in Liu et al. (2023a) (see also Childress et al. 2013, 2014; Maguire et al. 2014), we fit the Si II and Ca II IRT features with multiple Gaussian profiles. We find that modeling the Ca II IRT absorption requires two distinct velocity components—the photospheric-velocity features (PVFs) and the high-velocity features (HVFs). In Table 5 we list the estimates of the expansion velocities and the pseudo-equivalent widths (pEWs) of the major absorption lines from -12 to $+9$ days. In Figure 6 we show the peak absolute magnitude in the B band ($M_{B,\max}$) versus the velocity and pEW of Si II for SN 2022joj and a sample of normal SNe Ia from Zheng et al. (2018) and Burrow

et al. (2020). Figure 6 highlights that SN 2022joj has a normal $M_{B,\max}$ with a relatively low Si II $\lambda 6355$ expansion velocity (hereafter $v_{\text{Si II}}$). The Si II $\lambda 5972$ and Si II $\lambda 6355$ pEWs in SN 2022joj are smaller than those for most normal SNe Ia. In fact, SN 2022joj sits at the extreme edge of the shallow-silicon group proposed in Branch et al. (2006), which mainly consists of overluminous 91T-like/99aa-like objects. This is consistent with the high luminosity and blue color of SN 2022joj at maximum light, since a high photometric temperature results in higher ionization, reducing the abundance of singly ionized atoms (e.g., Si II). Interestingly, the pEW of Si II $\lambda 6355$ near peak is significantly smaller than that in the first spectrum. In typical 91T-like/99aa-like objects, the Si II features are weak or undetectable at early times because the ejecta are even hotter, and these features only start to emerge around maximum light (Filippenko et al. 1992b). In the early spectrum of SN 2022joj, in contrast, stronger absorption features from singly ionized Si

and Ca indicate a cooler line-forming region at early times compared to that at maximum brightness.

Prominent C II features are also detected in the overluminous SN 2003fg-like (03fg-like; Howell et al. 2006) SNe³² at their maximum brightness. However, 03fg-like objects show blue colors in the early light curves (Taubenberger et al. 2019) and appear even brighter in near-UV compared to normal SNe Ia at peak (Brown et al. 2014), unlike SN 2022joj. Many 03fg-like objects also show strong oxygen features in both their maximum-light and late-time spectra (Taubenberger et al. 2019), while in SN 2022joj, we do not find evidence for oxygen. Consequently, the explosion mechanism as well as the origin of carbon in SN 2022joj is likely very different from that of 03fg-like objects.

In conclusion, the spectral evolution of SN 2022joj shows some similarities to that of 91T-like/99aa-like objects, as well as peculiarities. A reasonable model to explain SN 2022joj needs to reproduce (i) a strong suppression in flux blueward of ~ 5000 Å at early times followed by a rapid evolution to blue colors; (ii) the seemingly contradictory observables at peak, namely the 4200 Å features similar to the Ti-trough in 91bg-like objects and the blue continuum/shallow Si II feature at maximum, which indicate low and high photometric temperatures, respectively; and (iii) prominent C II features at maximum brightness.

3.4. Host Galaxy Properties

We model the observed spectral energy distribution (SED; photometry in HSC-SSP *grizy* and LS W_1 filters) with the software package *Prospector*³³ version 1.1 (Johnson et al. 2021). The LS *grz* photometry, which is consistent with the HSC-SSP results but has a lower S/N, is excluded from this modeling. We assume a Chabrier initial-mass function (Chabrier 2003) and approximate the star formation history (SFH) by a linearly increasing SFH at early times followed by an exponential decline at late times (functional form $t \times \exp(-t/\tau)$, where t is the age of the SFH episode and τ is the e -folding timescale). The model is attenuated with the Calzetti et al. (2000) model. The priors of the model parameters are set identically to those used by Schulze et al. (2021).

The SED is adequately described by a galaxy template with a mass of $\log(M_*/M_\odot) = 7.13^{+0.15}_{-0.28}$, suggesting that the host is a dwarf galaxy. The modeled star formation rate (SFR) is consistent with 0, but we note that measuring low SFRs with SED fitting is not robust and is subject to systematics (Conroy 2013). In addition, the H α emission detected in the late-time spectrum of the SN (Section 2.2) indicates at least some level of star formation in the host.

4. Discussion

4.1. SN 2022joj Compared to Model Explosions

There are several physical mechanisms that can produce blue colors during the early evolution of SNe Ia, including heating

of the SN ejecta following the decay of radioactive ^{56}Ni , interaction of the SN ejecta with a nondegenerate companion (e.g., Kasen 2010), collisions between the SN ejecta and circumstellar material (e.g., Piro & Morozova 2016), strong mixing that surfaces ^{56}Ni to the outermost layers of the ejecta (e.g., Piro & Nakar 2013; Magee & Maguire 2020), and the production of radioactive isotopes in the detonation of a helium shell on the surface of the exploding WD (e.g., Noebauer et al. 2017; Polin et al. 2019).

In contrast, there are few proposed scenarios that can produce red colors up to a week after explosion, as in the case of SN 2022joj. If the newly synthesized ^{56}Ni is strongly confined to the innermost SN ejecta, then the SN may remain red for several days after explosion as the heating diffuses out toward the photosphere (Piro & Morozova 2016). Even the most confined ^{56}Ni configuration considered in Piro & Morozova (2016) converges to blue colors, similar to explosions with more extended ^{56}Ni distributions, within ~ 6 days of the explosion. SN 2022joj is observed to have very red colors ~ 7 days after t_{H} (meaning more than 7 days after explosion, since SNe Ia have a “dark phase” before photons diffuse out of the ejecta; Piro & Nakar 2013). Dessart et al. (2014) considered more realistic delayed-detonation scenarios. Some of their 1D unmixed delayed-detonation models still show a red $B - R$ color ($B - R \gtrsim 0.5$ mag) 7 days after the explosion (see the DDC20, DDC22, and DDC25 models in their Figure 1), comparable to that of SN 2022joj. However, these models never appear as blue as SN 2022joj at peak ($B - R \simeq 0.0$ mag), and the ^{56}Ni yields are relatively low ($M_{\text{Ni}56} \lesssim 0.3 M_\odot$), so they would result in subluminal events. In addition, we do not know any multidimensional explosion models that fail to produce any ^{56}Ni mixing within the ejecta, and therefore disfavor this scenario.

Alternatively, in the double-detonation scenario, a layer of IGEs in the ashes of the helium shell can produce significant opacity in the outer layers of the bulk ejecta, producing a red color (Polin et al. 2019). This scenario has been proposed for a few normal-luminosity SNe with red colors at early times, including SN 2016jhr (Jiang et al. 2017) and SN 2018aoz (Ni et al. 2022). In Figure 7 we compare the spectra of SN 2022joj at -12 days and $+0$ days with 1D double-detonation models from Polin et al. (2019) and 2D double-detonation models from Shen et al. (2021b). To create synthetic spectra, both models use *Sedona* (Kasen et al. 2006), a multidimensional radiative transfer (RT) simulator that assumes local thermodynamic equilibrium (LTE).

In the 1D models, the most important parameters are the mass of the C/O core (M_c) and the mass of the helium shell (M_s). The maximum luminosity depends on the amount of ^{56}Ni synthesized in the explosion, which is predominantly determined by the total progenitor mass ($M_c + M_s$; Polin et al. 2019). We find that the maximum brightness in the B band ($M_{B,\text{max}} = -19.46$ mag) is reproduced by the 1D models with relatively massive progenitors ($\sim 1.1 M_\odot$). However, models with such massive progenitors tend to produce blue, featureless spectra at early times (e.g., the $M_c = 1.1 M_\odot$, $M_s = 0.05 M_\odot$ model in Figure 7), inconsistent with the observations. Less massive models provide a better match to the line blanketing seen in the early spectra, but fail to reproduce the maximum brightness as well as the 4200 Å features in the observed spectra. The 1D models overestimate the pEW and the expansion velocity of the Si II $\lambda 6355$ line at peak. As a

³² This subclass is also referred to as “super- M_{Ch} ” SNe or SN 2009dc-like (Taubenberger et al. 2011) SNe.

³³ *Prospector* uses the Flexible Stellar Population Synthesis (FSPS) code (Conroy et al. 2009) to generate the underlying physical model and *python-fsps* (Foreman-Mackey et al. 2014) to interface with FSPS in *python*. The FSPS code also accounts for the contribution from the diffuse gas based on the *Cloudy* models from Byler et al. (2017). We use the dynamic nested sampling package *dynesty* (Speagle 2020) to sample the posterior probability.

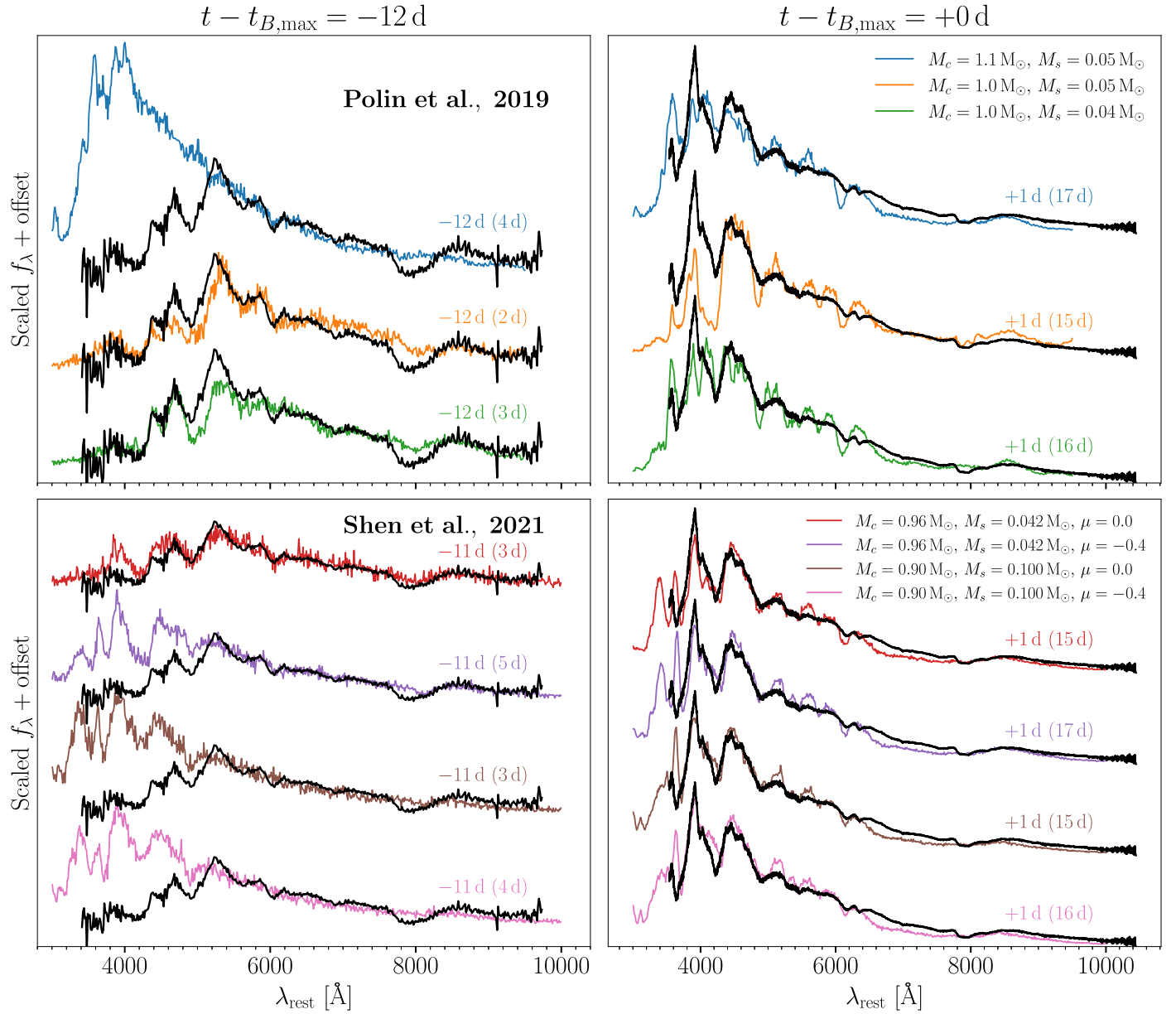


Figure 7. Comparisons of an early spectrum (-12 days) and a maximum-light spectrum ($+0$ days) of SN 2022joj (black) with two sets of double-detonation models. For each synthetic spectrum, the phase relative to $t_{B,\text{max}}$ is listed (the time since explosion is shown in parentheses). Top: comparison with 1D models from Polin et al. (2019) with different C/O core (M_c) and He shell (M_s) masses. Bottom: comparison with 2D models from Shen et al. (2021b) with different masses and viewing angles μ . The observed spectra have been corrected for Galactic extinction.

reference, we overplot the theoretical $M_{B,\text{max}}-v_{\text{Si II}}$ relation of 1D double-detonation models for thin helium shells ($M_s \simeq 0.01 M_{\odot}$) across a spectrum of progenitor masses in Polin et al. (2019) as a dashed black curve in the left panel of Figure 6, which is not in agreement with the properties of SN 2022joj. Besides, none of the models produce detectable C II features in the spectra at peak.

While the 1D models do not fully reproduce the observed properties of SN 2022joj, some of these tensions can be resolved when considering viewing-angle effects in multi-dimensional models. In Figure 6 we also show the properties of three 2D double-detonation models from Shen et al. (2021b) with a variety of M_c and M_s . For consistency in comparing the synthetic brightness with the observations of SN 2022joj, of which the K -corrections are unknown, the synthetic fluxes in the B filter of these models are evaluated after shifting the

synthetic spectra to $z = 0.02736$, the redshift of SN 2022joj. We obtain the Si II line properties using the same fitting techniques in Section 3.3.³⁴ We again find that more massive progenitors generally lead to higher-luminosity SNe, but different viewing angles produce significantly different spectral properties as a result of the asymmetry of the ejecta—materials closer to the point of helium ignition are less dense and expand faster (Shen et al. 2021b). In the plot, the cosine value of the polar angle relative to the point of helium ignition, μ , ranges from $+0.93$ (near the helium ignition point) to -0.93 (opposite

³⁴ The $v_{\text{Si II}}$ is systematically higher than the values displayed in Figure 20 of Shen et al. (2021b). In Shen et al. (2021b), $v_{\text{Si II}}$ is determined using the minimum of the Si II $\lambda 6355$ absorption without subtracting the continuum, such that the estimated minimum is systematically redshifted with respect to the actual line center, whereas we fit the absorption features with Gaussian profiles on top of a linear continuum.

to the helium ignition point). When the SN is observed along a line of sight closer to the detonation point in the shell (greater μ), it will appear fainter at maximum brightness and show a higher line velocity in Si II $\lambda 6355$. For a relatively high progenitor mass ($\gtrsim 1.1 M_{\odot}$), a high $v_{\text{Si II}}$ ($\gtrsim 13,500 \text{ km s}^{-1}$) is predicted in 1D models. However, all of the 2D models with $\mu \lesssim 0$ show a lower $v_{\text{Si II}}$ ($\lesssim 12,000 \text{ km s}^{-1}$), much closer to that of SN 2022joj in the $M_{B,\text{max}}-v_{\text{Si II}}$ phase space. Models with $\mu > 0$ are more consistent with 1D model predictions. It is suggested by Polin et al. (2019) that high-velocity SNe that follow the dashed line in Figure 6 result from sub- M_{Ch} double detonations, while SNe in the clump centered at $M_{B,\text{max}} \simeq -19.5$ mag and $v_{\text{Si II}} \simeq 11,000 \text{ km s}^{-1}$ are likely to be near- M_{Ch} explosions. Based on the 2D models, however, we should expect a similar number of high-velocity and normal-velocity double-detonation SNe Ia. A substantial fraction of the objects within the clump in the $M_{B,\text{max}}-v_{\text{Si II}}$ diagram may be sub- M_{Ch} double-detonation events viewed from certain orientations (Shen et al. 2021b). SN 2018aoz is a double-detonation candidate that, like SN 2022joj, exhibits early red colors before evolving to normal luminosity and blue colors (Ni et al. 2022). Interestingly, SN 2018aoz also resides in the high-luminosity, low-velocity clump in the $M_{B,\text{max}}-v_{\text{Si II}}$ space (Ni et al. 2023), and thus, it too may be an example of a double-detonation SN Ia viewed from the hemisphere opposite to the helium ignition point.

In the bottom panels of Figure 7 we show two 2D double-detonation models (each with two viewing angles) with a total progenitor mass of $\sim 1 M_{\odot}$ from Shen et al. (2021b). These models qualitatively match the observed spectra at maximum light. In the $M_c = 0.96 M_{\odot}$, $M_s = 0.042 M_{\odot}$ model, we find that when $\mu = 0$ (as viewed from the equator), it predicts a reasonable level of line blanketing in the blue side of the spectrum at early times (lower-left panel of Figure 7). Near maximum brightness, the model also reproduces the overall shape of the observed spectrum, though the strength of nearly all the absorption lines (4200 Å features, Si II, and Si II) is overestimated, and $v_{\text{Si II}}$ is also overestimated ($\sim 12,000 \text{ km s}^{-1}$). When viewed from the hemisphere opposite to the helium ignition point (e.g., $\mu = -0.4$), the model yields an asymmetric profile of 4200 Å features that matches the observations better. The Si II features are also predicted to be shallower, though still not as shallow as those in the observations. Nonetheless, the spectra at early times are expected to be much bluer than the observations. The $M_c = 0.90 M_{\odot}$, $M_s = 0.100 M_{\odot}$ models, especially when $\mu = -0.4$, produce even shallower and slower-expanding Si II features at maximum brightness. This is in agreement with the trend observed in the right panel of Figure 6: models with a thicker helium shell tend to exhibit shallower Si II features. However, the level of line blanketing blueward of ~ 5000 Å is also underestimated at early times. In addition, none of the models produce significant C II features, though we will show in Section 4.3 that this discrepancy does not necessarily invalidate the double-detonation interpretation.

To investigate the origin of the 4200 Å features at maximum luminosity, we run additional 1D Sedona RT simulations for the $M_c = 0.96 M_{\odot}$ and $M_s = 0.042 M_{\odot}$ model from Boos et al. (2021; adopted in the calculations of Shen et al. 2021b). The synthetic spectra are displayed in Figure 8. We adopt the density and chemical profile of the slice between the viewing angles $\mu = -0.467$ and $\mu = -0.333$ in the 2D ejecta at $t_{B,\text{max}}$

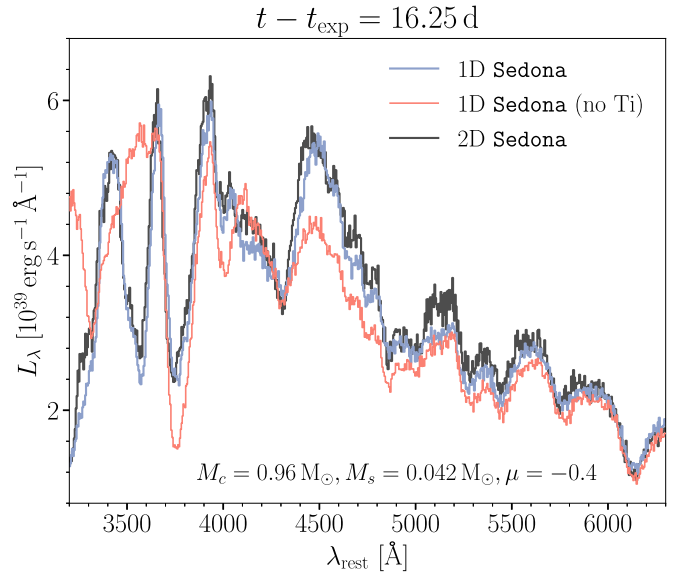


Figure 8. Comparison of the Sedona synthetic spectra at maximum luminosity indicates that Ti dominates the 4200 Å features in a double-detonation model. Two 1D Sedona models (blue + salmon pink) are run using the density and chemical profile of a slice between the viewing angles $\mu = -0.467$ and $\mu = -0.333$ of the $M_c = 0.96 M_{\odot}$ and $M_s = 0.042 M_{\odot}$ model from Boos et al. (2021). While the synthetic spectrum in the original 2D Sedona model can be well reproduced in a 1D run (blue), the model with all the titanium isotopes removed (salmon pink) cannot reproduce the remarkable 4200 Å features and exhibits a peak at ~ 4100 Å.

estimated in the original 2D RT simulations (16.25 days after the explosion) as the input of the 1D model. The synthetic spectrum is generally consistent with the 2D RT outcomes with a viewing angle $\mu = -0.4$. Then we run another 1D simulation with all the titanium isotopes in the slice removed. The resultant synthetic spectrum is still broadly consistent with the 1D and 2D results redward of ~ 5000 Å but shows a significant peak at ~ 4100 Å resembling those in normal SNe Ia. This indicates that in an explosion that yields an extended titanium distribution in the ejecta (such as the example double-detonation model shown here), a blend of Ti lines reshapes the spectrum around 4200 Å leading to the absence of a peak at ~ 4100 Å and a deep, asymmetric absorption feature.

The extremely red UV – optical colors near the maximum luminosity are also broadly consistent with the double-detonation scenario, since the heavy elements (e.g., Ti, V, Cr, and Fe) in the outer ejecta could effectively absorb the UV photons with wavelengths around 3000 Å. However, no existing models could accurately model the UVOT light curves, especially in the u band (~ 3100 – 3900 Å in the observed frame, or ~ 3000 – 3800 Å in the rest frame of the host galaxy), where the flux is dominated by the reemission of Ti, V, and Cr, and non-LTE effects could be important.

While none of the models presented here provide a strong match to SN 2022joj at every phase, we draw the broad conclusion that the spectroscopic properties of SN 2022joj are qualitatively consistent with a sub- M_{Ch} WD ($\gtrsim 1.0 M_{\odot}$) double detonation viewed from the hemisphere opposite to the ignition point. Observers from such a viewing angle would observe strong absorption features in the blue portion of the spectrum dominated by Ti as well as relatively shallow and slowly expanding Si lines in the red portion. We emphasize that none of the models considered here was specifically developed and tuned to explain SN 2022joj. Customized models specifically

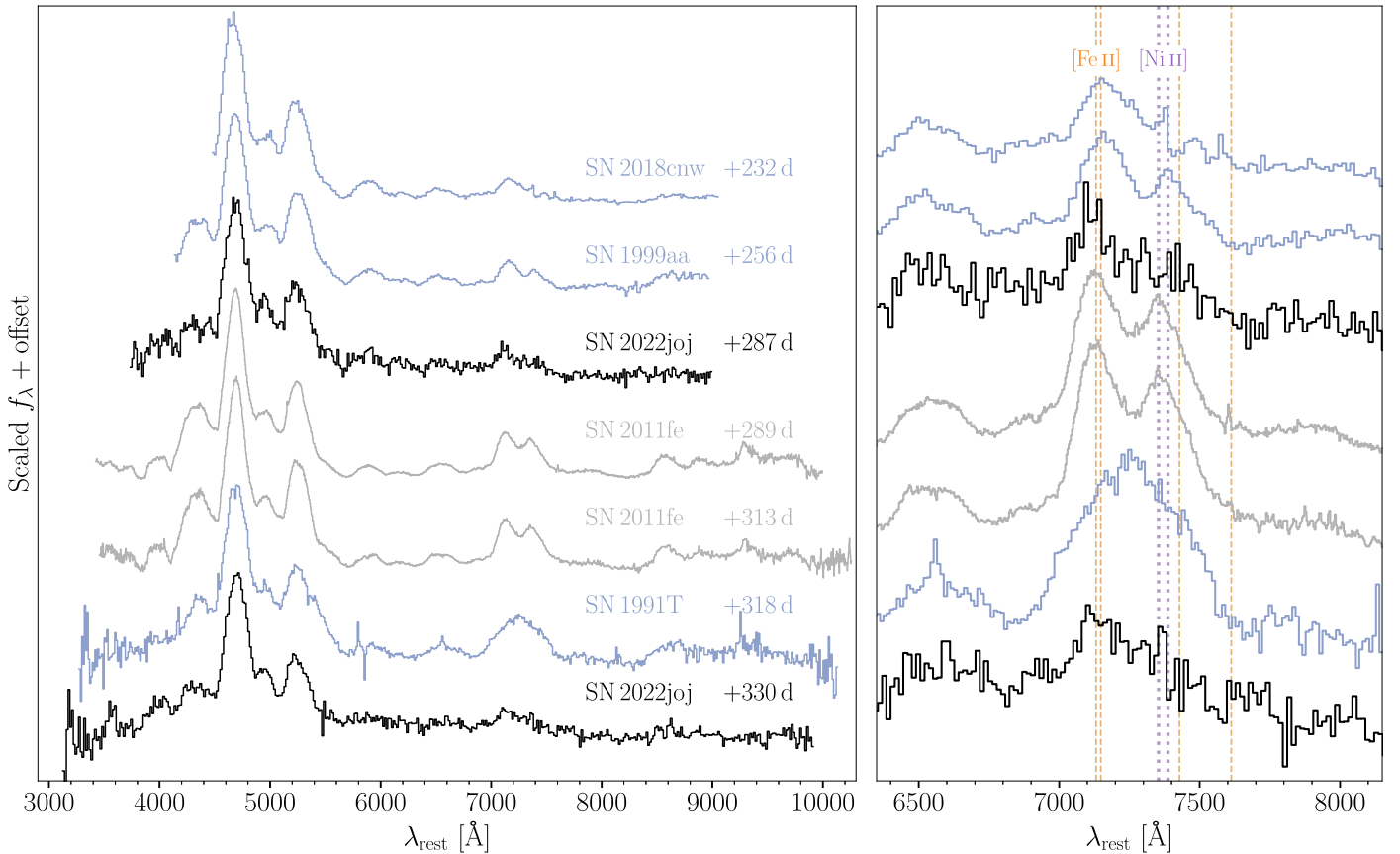


Figure 9. Nebular-phase spectra of SN 2022joj (black); three overluminous SNe Ia (blue), SN 1991T, SN 1999aa, and SN 2018cnw; and a normal SN Ia (gray), SN 2011fe. The right panel zooms in on the features around 7300 Å. The flux has been normalized to the [Fe III] features around 4700 Å. The orange dashed lines correspond to the wavelengths of four [Fe II] lines (7155, 7172, 7453, and 7638 Å), while the purple dotted lines correspond to the wavelengths of two [Ni II] lines (7378 and 7412 Å), both blueshifted by 1000 km s⁻¹. The spectra were downloaded from WiseREP (Yaron & Gal-Yam 2012), with the following original data sources: SN 1991T and SN 1999aa—Silverman et al. (2012); SN 2011fe—Mazzali et al. (2015); SN 2018cnw—this work.

tuned for SN 2022joj may reproduce all the observed features simultaneously, and we suggest more 2D double-detonation simulations should be performed. Furthermore, additional improvements can be made via an improved handling of the RT (e.g., non-LTE effects; see Shen et al. 2021a).

4.2. The 7300 Å Region in the Nebular-phase Spectra

In Figure 9 we compare the two nebular-phase spectra of SN 2022joj with those of the overluminous SNe Ia (SN 1991T, SN 1999aa, and SN 2018cnw) and the normal-luminosity SN 2011fe.

Compared to those of other SNe Ia, the nebular spectra of SN 2022joj show a relatively low flux ratio between the complex at ~ 7300 Å (hereafter the 7300 Å features) dominated by [Fe II] and [Ni II] and the complex at ~ 4700 Å dominated by [Fe III]. This suggests high ionization in the ejecta (Wilk et al. 2020). In addition to the lower flux ratio, the profile of the 7300 Å features in SN 2022joj is also distinct from that of other SNe. Most SNe Ia show a bimodal structure in their 7300 Å features (e.g., Graham et al. 2017; Maguire et al. 2018). The bluer peak is dominated by [Fe II] $\lambda\lambda 7155, 7172$, while [Ni II] $\lambda\lambda 7378, 7412$ usually have nonnegligible contributions to the redder peak (see Figure 9). In some peculiar SNe Ia (mostly subluminous ones), the detection of [Ca II] $\lambda\lambda 7291, 7324$ has also been reported (e.g., Jacobson-Galán et al. 2020; Siebert et al. 2020). The bimodal morphology is prominent in the spectra of SN 1999aa and SN 2011fe. SN 1999T is well known

for its broader emission lines in the nebular phase, so the composition of the 7300 Å features is ambiguous. In the spectra of SN 2022joj and SN 2018cnw, however, the redder peak is absent and the 7300 Å features show an asymmetric single peak, which seems to indicate a low abundance of Ni in the ejecta.

To investigate the relative contributions of [Fe II] and [Ni II] to the 7300 Å features in SN 2022joj, we model this region with multiple Gaussian emission profiles using the same technique in Section 3.3. We include four [Fe II] lines (7155, 7172, 7388, and 7453 Å) and two [Ni II] lines (7378 and 7412 Å) in the fit. For each species, the relative flux ratios of lines are fixed, whose values are adopted from Jerkstrand et al. (2015). For [Fe II], we set $L_{7155}:L_{7172}:L_{7388}:L_{7453} = 1:0.24:0.19:0.31$, and for [Ni II], we set $L_{7378}:L_{7412} = 1:0.31$. These line ratios are calculated assuming LTE, but the departure from LTE should not be significant under the typical conditions in the ejecta (Jerkstrand et al. 2015). We allow the amplitudes A of these Gaussian profiles to be either positive or negative. The velocity dispersions σ_v in different lines of each species are set to be the same. For both A and $\log \sigma_v$, we adopt flat priors, and only allow σ_v to vary between 1000 and 6000 km s⁻¹. In addition, we adopt wide Gaussian priors for the radial velocities v of [Fe II] and [Ni II], both centered at -1000 km s⁻¹ with a standard deviation of 2000 km s⁻¹. The fitted models are shown in Figure 10, where the colored

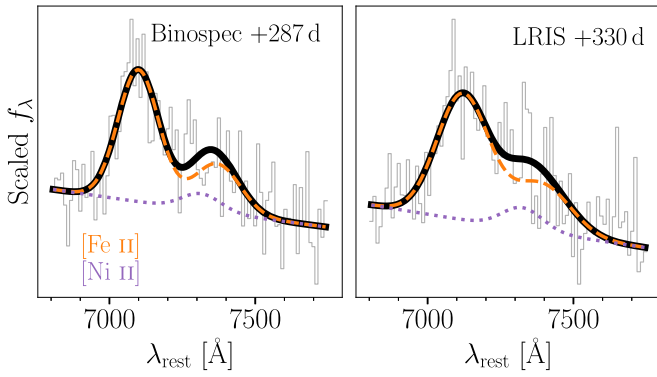


Figure 10. Fits to the 7300 Å region containing [Fe II] and [Ni II] features are consistent with a low Ni II abundance. The observed spectra are shown in gray. The colored lines correspond to the models of [Fe II] (orange) and [Ni II] (purple) features. For the model parameters we adopt the mean values of their posterior distributions. The black solid lines are the overall models.

curves correspond to the [Fe II] and [Ni II] emission adopting the mean values of the posterior distributions of the model parameters sampled with MCMC. The fitted parameters are listed in Table 6. In both spectra, the flux of [Ni II] is consistent with 0 ($L_{[\text{Ni II}] \lambda 7378}/L_{[\text{Fe II}] \lambda 7155} = 0.13 \pm 0.14$ at +287 days and 0.18 ± 0.16 at +330 days; the flux ratios of lines are estimated with the ratios of their pEWs, and the uncertainties are the robust standard deviations estimated with the median absolute deviation of the drawn sample). We also find that the [Ni II] velocities cannot be constrained by the data, whose uncertainties estimated in both spectra are greater than the standard deviations of their Gaussian priors (2000 km s^{-1}), again disfavoring a solid [Ni II] detection. The 7300 Å features can be well fit with [Fe II] emission only. In addition, we test fitting this complex with [Ca II] in addition to [Fe II] and [Ni II], but find no evidence for [Ca II].

The relative abundance of Ni and Fe, which probes the mass of the progenitor WD, can be estimated via the flux ratio of their emission lines. At >300 days after explosion ^{56}Fe is the dominant isotope of Fe following the decay of ^{56}Ni through the chain $^{56}\text{Ni} \rightarrow ^{56}\text{Co} \rightarrow ^{56}\text{Fe}$. Consequently, the Fe abundance primarily depends on the yield of ^{56}Ni . The Ni abundance, however, is sensitive to both the progenitor mass and the explosion scenario. The stable Ni isotopes (^{58}Ni , ^{60}Ni , and ^{62}Ni) are more neutron-rich compared to the α -species ^{56}Ni , and can only be formed in high-density regions with an enhanced electron capture rate during the explosion (Nomoto 1984; Khokhlov 1991). Consequently, SNe Ia from sub- M_{Ch} WDs, with central densities that are lower than those of near- M_{Ch} WDs, are expected to show a lower abundance of stable Ni isotopes (Iwamoto et al. 1999; Seitenzahl et al. 2013; Shen et al. 2018b).

To estimate the relative abundance of Ni and Fe, we use the equation adopted in Jerkstrand et al. (2015) and Maguire et al. (2018),

$$\frac{L_{7378}}{L_{7155}} = 4.9 \frac{n_{\text{Ni II}}}{n_{\text{Fe II}}} \exp\left(\frac{0.28 \text{ eV}}{k_B T}\right) \frac{dc_{\text{Ni II}}}{dc_{\text{Fe II}}}, \quad (1)$$

where L_{7378}/L_{7155} is the flux ratio of the [Ni II] $\lambda 7378$ line to the [Fe II] $\lambda 7155$ line, $n_{\text{Ni II}}/n_{\text{Fe II}}$ is the number density ratio of Ni II and Fe II, and $dc_{\text{Ni II}}/dc_{\text{Fe II}}$ is the ratio of the departure coefficients from LTE for these two ions. Since both Ni II and Fe II are singly ionized species with similar ionization

potentials, we assume that $n_{\text{Ni II}}/n_{\text{Fe II}}$ is a good approximation of the total Ni/Fe ratio. As illustrated in Maguire et al. (2018), this assumption proves to be valid by modeling nebular-phase spectra at similar phases (Fransson & Jerkstrand 2015; Shingles et al. 2022), with the relative deviation from the ionization balance $\lesssim 20\%$. We handle uncertainties due to the unknown temperature, the ratio of departure coefficients, and the ionization balance in a Monte Carlo way. We randomly generate $N = 4000$ samples of the temperature (3000–8000 K), the ratio of departure coefficients (1.2–2.4), and the ionization balance factor (0.8–1.2) assuming uncorrelated uniform distributions. These intervals are again adopted from Maguire et al. (2018). Combining these quantities with the samples of line profile parameters drawn with the MCMC, we obtain N estimates of Ni/Fe, which are effectively drawn from its posterior distribution. We find that Ni/Fe is consistent with 0 and we obtain a 3σ upper limit of $\text{Ni/Fe} < 0.03$. Such a low Ni abundance is more consistent with the yields of sub- M_{Ch} double-detonation scenarios (Shen et al. 2018b), much lower than the expected outcomes of near- M_{Ch} , delayed-detonation models (Seitenzahl et al. 2013) and pure deflagration models (Iwamoto et al. 1999).

Alternatively, it is proposed in Blondin et al. (2022) that for high-luminosity SNe Ia, the absence of [Ni II] lines can be a result of high ionization of Ni in the inner ejecta, despite the fact that a significant amount of Ni exists. It is shown that the [Ni II] $\lambda\lambda 7378, 7412$ lines can be strongly suppressed even in a high-luminosity, near- M_{Ch} delayed-detonation model, once the Ni II/Ni III ratio at the center of the ejecta is artificially reduced by a factor of 10. Nevertheless, it remains to be questioned whether a physical mechanism exists to boost the ionization in the inner ejecta, where stable Ni dominates the radioactive ^{56}Ni and ^{56}Co , and the deposited energy per particle due to the radioactive decay is usually low. One possible scenario is inward mixing, which brings ^{56}Co into the innermost ejecta such that the ionization would significantly increase. However, in this case calcium would inevitably be mixed inward as well, and the resultant Ca II $\lambda\lambda 7291, 7324$ lines would stand out and dominate the 7300 Å features (Blondin et al. 2022). Other physical mechanisms are thus required to reduce the Ni II/Ni III ratio at the center of a near- M_{Ch} explosion.

We also find that the [Fe II] lines are significantly blueshifted ($v_{[\text{Fe II}]} = -(2.46 \pm 0.38) \times 10^3 \text{ km s}^{-1}$ at +287 days and $-(1.56 \pm 0.60) \times 10^3 \text{ km s}^{-1}$ at +330 days). This is consistent with other SNe Ia showing low $v_{\text{Si II}}$ at maximum brightness (Maeda et al. 2010a; Maguire et al. 2018; Li et al. 2021), and also in qualitative agreement with the asymmetric sub- M_{Ch} double-detonation scenario. Specifically, along a line of sight opposite to the shell detonation point, observers would see intermediate-mass elements (IMEs) with low expansion velocities, including Si II. In the meantime, the IGEs at the center of the ejecta would have a bulk velocity toward the observer (see Figures 1 and 2 of Bulla et al. 2016; see also Fink et al. 2010).

4.3. Carbon Features at Maximum Luminosity

The spectrum at maximum luminosity exhibits strong C II $\lambda\lambda 6580, 7234$ lines at a velocity of $\sim 10,000 \text{ km s}^{-1}$ (Figure 11). In the −12 days spectrum, we do not find strong evidence for the C II $\lambda 6580$ line, though there is an absorption

Table 6
Fits to the Late-time Spectra around 7300 Å with [Fe II] and [Ni II] Emission

Phase (days)	[Fe II] $\lambda 7155$			[Ni II] $\lambda 7378$		
	v (10^3 km s^{-1})	σ_v (10^3 km s^{-1})	pEW (Å)	v (10^3 km s^{-1})	σ_v (10^3 km s^{-1})	pEW (Å)
+286.8	-2.46 ± 0.38	2.98 ± 0.47	-129 ± 25	-2.89 ± 2.60	3.02 ± 1.45	-14 ± 19
+329.8	-1.56 ± 0.60	3.84 ± 0.80	-113 ± 28	-2.49 ± 2.44	3.11 ± 1.41	-13 ± 22

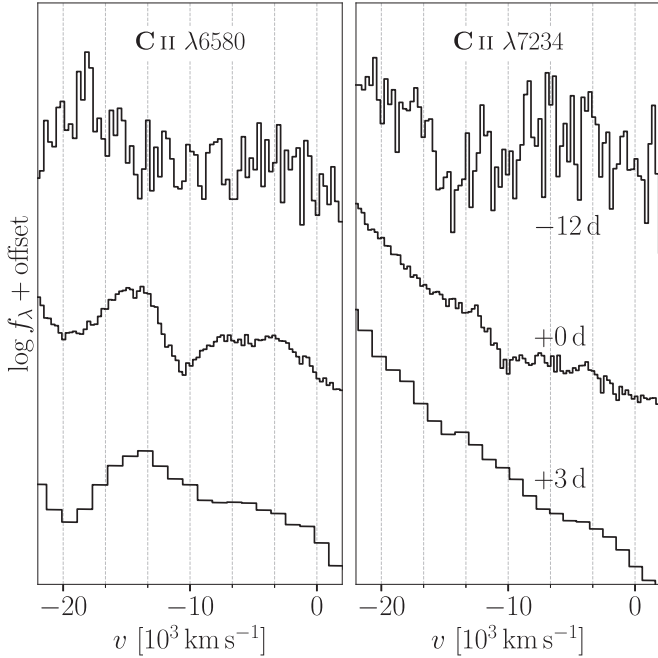


Figure 11. Prominent C II $\lambda\lambda 6580, 7234$ absorption lines at maximum luminosity. No evident C II $\lambda 6580$ lines are found in the earliest spectrum (-12 days; though there is one absorption feature that might be associated with C II $\lambda 7234$ at $\sim 14,000 \text{ km s}^{-1}$) or in the post-maximum spectrum ($+3$ days). All spectra are binned with a bin size of 5 Å , except for the low-resolution SEDM spectrum ($+3$ days). The dashed lines correspond to the wavelengths of the C II lines assuming a range of velocities.

feature that might be associated with the C II $\lambda 7234$ line at an expansion velocity of $\sim 14,000 \text{ km s}^{-1}$ (see the right panel in Figure 11). The feature shows a velocity dispersion that is a factor of ~ 3 greater than that of the unambiguous C II $\lambda 7234$ line at maximum luminosity, and its nature remains vague. In this section we briefly discuss the possible origin of the carbon features.

In double detonations of sub- M_{Ch} WDs, the burning of carbon is expected to be efficient, with only a small fraction of carbon left unburnt. In 1D double-detonation models from Polin et al. (2019), only a negligible ($\lesssim 10^{-5} M_{\odot}$) amount of carbon is unburnt in normal and overluminous SNe, which should not cause any noticeable spectroscopic features. Multi-dimensional simulations produce a greater amount ($\sim 10^{-4}$ – $10^{-3} M_{\odot}$) of leftover carbon (Fink et al. 2010; Boos et al. 2021), which is still roughly 2 orders of magnitude lower than the yields of IMEs. Nevertheless, most of the unburnt carbon will be concentrated on the surface of the C/O core, forming a sharp carbon-rich shell (see Figures 5–8 in Boos et al. 2021) with a high expansion velocity ($> 10,000 \text{ km s}^{-1}$). Both 1D and 2D double-detonation models have low carbon yields in the helium ashes, so the carbon features may be strengthened over time, as the photosphere moves inward to the

carbon-rich regions. Nevertheless, with the current resolution in the RT simulations, the contribution of such a sharp shell is unlikely to be captured in the resultant synthetic spectra.

Another possible origin of unburnt carbon in a double-detonation SN is the stripped material from a degenerate companion. In the dynamically driven double-degenerate double-detonation (D^6) model (Shen et al. 2018a), the primary C/O WD could detonate following the dynamical ignition of a helium shell from its WD companion (either a helium WD or a C/O WD with a substantial helium envelope) during the unstable mass transfer (Guillochon et al. 2010; Pakmor et al. 2013). In this case, a significant amount ($\sim 10^{-3} M_{\odot}$) of materials can be stripped from the C/O WD companion, following the explosion of a $1 M_{\odot}$ primary WD (Tanikawa et al. 2018; S. J. Boos et al. 2023, in preparation), although the amount of carbon would likely be significantly less if the companion still holds a substantial helium envelope (Tanikawa et al. 2019). The velocity of the stripped carbon is expected to be low (e.g., centered at $\sim 3000 \text{ km s}^{-1}$ in Tanikawa et al. 2018), though more studies will need to be done to test the robustness of this estimate.

Explosion mechanisms that would result in a greater amount of unburnt carbon in the ejecta include the pure deflagration (Nomoto et al. 1984) or pulsating delayed detonation (Hoeftlich et al. 1995; Dessart et al. 2014) of a near- M_{Ch} WD, and the violent merger of binary WDs (Raskin et al. 2014). None of these models reproduce the unusual red color in the early light curves or the peculiar spectroscopic features of SN 2022joj as well as the helium-shell double-detonation scenario does.

We conclude that while it remains to be questioned if double detonations could really produce strong carbon features, the detection of C II $\lambda\lambda 6580, 7234$ lines in SN 2022joj does not necessarily invalidate our hypothesis of its double-detonation origin.

5. Conclusions

We have presented observations of SN 2022joj, a peculiar SN Ia. SN 2022joj has an unusual color evolution, with a remarkably red $g_{\text{ZTF}} - r_{\text{ZTF}}$ color at early times due to continuous absorption in the blue portion of its SED. Absorption features observed around maximum light simultaneously suggest high (a blue continuum and shallow Si II lines similar to those of overluminous, 99aa-/91T-like SNe) and low (tentative Ti II features resembling those of subluminous, 91bg-like SNe) photospheric temperatures. The nebular-phase spectra of SN 2022joj suggest a high ionization and low Ni abundance in the ejecta, consistent with a sub- M_{Ch} explosion.

The early red colors are most likely due to a layer of IGEs in the outermost ejecta as products of a helium-shell detonation, in the sub- M_{Ch} double-detonation scenario. If the asymmetric ejecta are observed from the hemisphere opposite to the helium ignition point, we find that the resultant synthetic spectra could qualitatively reproduce some of the observed properties,

including (i) significant line blanketing of flux due to IGEs at early phases, (ii) strong absorption features around 4200 Å as well as relatively weak Si II features near maximum brightness, and (iii) blueshifted [Fe II] λ 7155 accompanied with a relatively low expansion velocity of Si II at peak. Current double-detonation models cannot reproduce the strong C II lines in SN 2022joj at its maximum luminosity, but the double-detonation hypothesis is not necessarily disfavored and an improved RT treatment will be needed in modeling the observational effects of unburnt carbon. No existing double-detonation model can fully explain all the observational properties of SN 2022joj. As a result, it is possible that some alternative model is superior, though we find that the early red colors are difficult to explain with alternative explosion scenarios. Further refinement of multidimensional models covering a finer grid of progenitor properties may answer the question if the peculiar SN 2022joj is really triggered by a double detonation.

Acknowledgments

We thank the anonymous referee for a thoughtful report. We are grateful to Ping Chen, Avishay Gal-Yam, Anthony Piro, Anna Ho, and Jiaxuan Li for fruitful discussions, as well as to Peter Blanchard and Jillian Rastinejad for the LRIS spectra they obtained. We thank UC Berkeley undergraduate students Kate Bostow, Cooper Jacobus, Gabrielle Stewart, Edgar Vidal, Victoria Brendel, Asia deGraw, Conner Jennings, and Michael May for the Lick/Nickel photometry. K.J.S. was in part supported by NASA/ESA Hubble Space Telescope (HST) programs #15871 and #15918. S.J.B. and D.M.T. acknowledge support from NASA grant HST-AR-16156. L.H. is funded by the Irish Research Council under grant GOIPG/2020/1387. K.M. is funded by the EU H2020 European Research Council (ERC) grant 758638. S.S. acknowledges support from the G.R.E.A.T. research environment, funded by *Vetenskapsrådet*, the Swedish Research Council, project 2016-06012. G.D. is supported by the H2020 ERC grant 758638. C. D.K. is partly supported by a Center for Interdisciplinary Exploration and Research in Astrophysics (CIERA) postdoctoral fellowship. A.V.F.'s supernova group at UC Berkeley received generous financial assistance from the Christopher R. Redlich Fund, from Briggs and Kathleen Wood (T.G.B. is a Wood Specialist in Astronomy), from Alan Eustace (W.Z. is a Eustace Specialist in Astronomy), and from numerous other donors.

We appreciate the excellent assistance of the staff at the observatories where data were obtained. This work is based on observations obtained with the Samuel Oschin Telescope 48 inch and the 60 inch Telescope at the Palomar Observatory as part of the ZTF project. ZTF is supported by the NSF under grant AST-2034437 and a collaboration including Caltech, IPAC, the Weizmann Institute of Science, the Oskar Klein Centre at Stockholm University, the University of Maryland, Deutsches Elektronen-Synchrotron and Humboldt University, the TANGO Consortium of Taiwan, the University of Wisconsin (UW) at Milwaukee, Trinity College Dublin, Lawrence Livermore National Laboratories, IN2P3, University of Warwick, Ruhr University Bochum, and Northwestern University. Operations are conducted by Caltech Optical Observatories, IPAC, and UW. The SED Machine is based upon work supported by the NSF under grant 1106171. The ZTF forced-photometry service was funded under the Heising-

Simons Foundation grant #12540303 (PI: Graham). The Gordon and Betty Moore Foundation, through both the Data-driven Investigator Program and a dedicated grant, provided critical funding for SkyPortal.

A major upgrade of the Kast spectrograph on the Shane 3 m telescope at Lick Observatory, led by Brad Holden, was made possible through generous gifts from the Heising-Simons Foundation, William and Marina Kast, and the University of California Observatories. KAIT and its ongoing operation were made possible by donations from Sun Microsystems Inc., the Hewlett-Packard Company, AutoScope Corporation, Lick Observatory, the U.S. NSF, the University of California, the Sylvia & Jim Katzman Foundation, and the TABASGO Foundation. Research at Lick Observatory is partially supported by a generous gift from Google.




This work is also based in part on observations made with the NOT, owned in collaboration by the University of Turku and Aarhus University, and operated jointly by Aarhus University, the University of Turku, and the University of Oslo (respectively representing Denmark, Finland, and Norway), the University of Iceland, and Stockholm University at the Observatorio del Roque de los Muchachos, La Palma, Spain, of the Instituto de Astrofísica de Canarias. The W. M. Keck Observatory is operated as a scientific partnership among the California Institute of Technology, the University of California, and NASA; the observatory was made possible by the generous financial support of the W. M. Keck Foundation. Observations reported here were obtained at the MMT Observatory, a joint facility of the Smithsonian Institution and the University of Arizona. W. M. Keck Observatory and MMT Observatory access was supported by Northwestern University and CIERA.

This work has made use of data from the ATLAS project, which is primarily funded to search for near-Earth objects (NEOs) through NASA grants NN12AR55G, 80NSSC18K0284, and 80NSSC18K1575; byproducts of the NEO search include images and catalogs from the survey area. This work was partially funded by Kepler/K2 grant J1944/80NSSC19K0112 and HST GO-15889, and STFC grants ST/T000198/1 and ST/S006109/1. The ATLAS science products have been made possible through the contributions of the University of Hawaii Institute for Astronomy, the Queen's University Belfast, the Space Telescope Science Institute, the South African Astronomical Observatory, and the Millennium Institute of Astrophysics (MAS), Chile.

Facilities: PO:1.2m (ZTF), Swift (UVOT), KAIT, Nickel, Liverpool:2m (IO:O), PO:1.5m (SEDM), FTN (FLOYDS), FTS (FLOYDS), NOT (ALFOSC), Liverpool:2m (SPRAT), Keck:I (LRIS), MMT (Binospec), Hale (TSpec).

Software: *astropy* (Astropy Collaboration et al. 2013, 2018), *dynesty* (Speagle 2020), *matplotlib* (Hunter 2007), *NumPy* (Harris et al. 2020), *prospector* (Johnson et al. 2021), *PyMC* (Salvatier et al. 2016), *PyPeIt* (Prochaska et al. 2020), *pysedm* (Rigault et al. 2019), *sncosmo* (Barbary et al. 2023), *Python-FSPP* (Conroy et al. 2009; Conroy & Gunn 2010; Foreman-Mackey et al. 2014), *Sedona* (Kasen et al. 2006), *ZFSP* (Masci et al. 2023).

ORCID iDs

Chang Liu (刘畅)  <https://orcid.org/0000-0002-7866-4531>
 Adam A. Miller  <https://orcid.org/0000-0001-9515-478X>
 Samuel J. Boos  <https://orcid.org/0000-0002-1184-0692>

Ken J. Shen  <https://orcid.org/0000-0002-9632-6106>
 Dean M. Townsley  <https://orcid.org/0000-0002-9538-5948>
 Steve Schulze  <https://orcid.org/0000-0001-6797-1889>
 Luke Harvey  <https://orcid.org/0000-0003-3393-9383>
 Kate Maguire  <https://orcid.org/0000-0002-9770-3508>
 Joel Johansson  <https://orcid.org/0000-0001-5975-290X>
 Thomas G. Brink  <https://orcid.org/0000-0001-5955-2502>
 Umut Burgaz  <https://orcid.org/0000-0003-0126-3999>
 Georgios Dimitriadis  <https://orcid.org/0000-0001-9494-179X>
 Alexei V. Filippenko  <https://orcid.org/0000-0003-3460-0103>
 Saarah Hall  <https://orcid.org/0000-0002-3841-380X>
 K-Ryan Hinds  <https://orcid.org/0000-0002-0129-806X>
 Andrew Hoffman  <https://orcid.org/0000-0002-8732-6980>
 Viraj Karambelkar  <https://orcid.org/0000-0003-2758-159X>
 Charles D. Kilpatrick  <https://orcid.org/0000-0002-5740-7747>
 Daniel Perley  <https://orcid.org/0000-0001-8472-1996>
 Neil Pichay  <https://orcid.org/0009-0009-7665-6827>
 Huei Sears  <https://orcid.org/0000-0001-8023-4912>
 Jesper Sollerman  <https://orcid.org/0000-0003-1546-6615>
 Robert Stein  <https://orcid.org/0000-0003-2434-0387>
 Jacco H. Terwel  <https://orcid.org/0000-0001-9834-3439>
 WeiKang Zheng  <https://orcid.org/0000-0002-2636-6508>
 Matthew J. Graham  <https://orcid.org/0000-0002-3168-0139>
 Mansi M. Kasliwal  <https://orcid.org/0000-0002-5619-4938>
 Leander Lacroix  <https://orcid.org/0000-0003-0629-5746>
 Josiah Purdum  <https://orcid.org/0000-0003-1227-3738>
 Benjamin Rusholme  <https://orcid.org/0000-0001-7648-4142>
 Avery Wold  <https://orcid.org/0000-0002-9998-6732>

References

- Aihara, H., Armstrong, R., Bickerton, S., et al. 2018, *PASJ*, **70**, S8
 Arbour, R., Papenkova, M., Li, W. D., Filippenko, A. V., & Armstrong, M. 1999, *IAUC*, **7156**, 1
 Astropy Collaboration, Price-Whelan, A. M., Sipőcz, B. M., et al. 2018, *AJ*, **156**, 123
 Astropy Collaboration, Robitaille, T. P., Tollerud, E., et al. 2013, *A&A*, **558**, A33
 Barbary, K., Bailey, S., Barentsen, G., et al. 2023, *SNCosmo*, v2.10.0, Zenodo, doi:10.5281/zenodo.7876632
 Bellm, E. C., Kulkarni, S. R., Barlow, T., et al. 2019a, *PASP*, **131**, 068003
 Bellm, E. C., Kulkarni, S. R., Graham, M. J., et al. 2019b, *PASP*, **131**, 018002
 Blagorodnova, N., Neill, J. D., Walters, R., et al. 2018, *PASP*, **130**, 035003
 Blondin, S., Bravo, E., Timmes, F. X., Dessart, L., & Hillier, D. J. 2022, *A&A*, **660**, A96
 Blondin, S., & Tonry, J. L. 2007, *ApJ*, **666**, 1024
 Boos, S. J., Townsley, D. M., Shen, K. J., Caldwell, S., & Miles, B. J. 2021, *ApJ*, **919**, 126
 Branch, D., Dang, L. C., Hall, N., et al. 2006, *PASP*, **118**, 560
 Branch, D., Thomas, R. C., Baron, E., et al. 2004, *ApJ*, **606**, 413
 Brown, P. J., Kuin, P., Scalzo, R., et al. 2014, *ApJ*, **787**, 29
 Brown, P. J., Perry, J. M., Beeny, B. A., Milne, P. A., & Wang, X. 2018, *ApJ*, **867**, 56
 Brown, T. M., Baliber, N., Bianco, F. B., et al. 2013, *PASP*, **125**, 1031
 Bulla, M., Miller, A. A., Yao, Y., et al. 2020, *ApJ*, **902**, 48
 Bulla, M., Sim, S. A., Kromer, M., et al. 2016, *MNRAS*, **462**, 1039
 Burrow, A., Baron, E., Ashall, C., et al. 2020, *ApJ*, **901**, 154
 Byler, N., Dalcanton, J. J., Conroy, C., & Johnson, B. D. 2017, *ApJ*, **840**, 44
 Calzetti, D., Armus, L., Bohlin, R. C., et al. 2000, *ApJ*, **533**, 682
 Carrick, J., Turnbull, S. J., Lavaux, G., & Hudson, M. J. 2015, *MNRAS*, **450**, 317
 Cenko, S. B., Fox, D. B., Moon, D.-S., et al. 2006, *PASP*, **118**, 1396
 Chabrier, G. 2003, *PASP*, **115**, 763
 Chambers, K. C., Magnier, E. A., Metcalfe, N., et al. 2016, arXiv:1612.05560
 Childress, M. J., Filippenko, A. V., Ganeshalingam, M., & Schmidt, B. P. 2014, *MNRAS*, **437**, 338
 Childress, M. J., Scalzo, R. A., Sim, S. A., et al. 2013, *ApJ*, **770**, 29
 Chu, M., Dahiwal, A., & Fremling, C. 2022, *TNSCR*, **36**, 1
 Conroy, C. 2013, *ARA&A*, **51**, 393
 Conroy, C., & Gunn, J. E. 2010, *ApJ*, **712**, 833
 Conroy, C., Gunn, J. E., & White, M. 2009, *ApJ*, **699**, 486
 Coughlin, M. W., Bloom, J. S., Nir, G., et al. 2023, *ApJS*, **267**, 31
 De, K., Kasliwal, M. M., Polin, A., et al. 2019, *ApJL*, **873**, L18
 De, K., Kasliwal, M. M., Tzanidakis, A., et al. 2020, *ApJ*, **905**, 58
 de los Reyes, M. A. C., Kirby, E. N., Seitenzahl, I. R., & Shen, K. J. 2020, *ApJ*, **891**, 85
 Dekany, R., Smith, R. M., Riddle, R., et al. 2020, *PASP*, **132**, 038001
 Dessart, L., Blondin, S., Hillier, D. J., & Khokhlov, A. 2014, *MNRAS*, **441**, 532
 Dey, A., Schlegel, D. J., Lang, D., et al. 2019, *AJ*, **157**, 168
 Dong, Y., Valenti, S., Polin, A., et al. 2022, *ApJ*, **934**, 102
 Duev, D. A., Mahabal, A., Masci, F. J., et al. 2019, *MNRAS*, **489**, 3582
 Eitner, P., Bergemann, M., Ruiter, A. J., et al. 2023, *A&A*, **677**, A151
 El-Badry, K., Shen, K. J., Chandra, V., et al. 2023, *OJAp*, **6**, 28
 Fabricant, D., Fata, R., Epps, H., et al. 2019, *PASP*, **131**, 075004
 Filippenko, A. V. 1982, *PASP*, **94**, 715
 Filippenko, A. V., Li, W. D., Treffers, R. R., & Modjaz, M. 2001, in *ASP Conf. Ser.* 246, IAU Coll. 183: Small Telescope Astronomy on Global Scales, ed. B. Paczynski, W.-P. Chen, & C. Lemme (San Francisco, CA: ASP), 121
 Filippenko, A. V., Richmond, M. W., Branch, D., et al. 1992a, *AJ*, **104**, 1543
 Filippenko, A. V., Richmond, M. W., Matheson, T., et al. 1992b, *ApJL*, **384**, L15
 Fink, M., Röpke, F. K., Hillebrandt, W., et al. 2010, *A&A*, **514**, A53
 Fitzpatrick, E. L. 1999, *PASP*, **111**, 63
 Flörs, A., Spyromilio, J., Taubenberger, S., et al. 2020, *MNRAS*, **491**, 2902
 Foreman-Mackey, D., Sick, J., & Johnson, B. 2014, *Python-Fsps: Python Bindings To Fsps (V0.1.1)*, v0.1.1, Zenodo, doi:10.5281/zenodo.12157
 Fransson, C., & Jerkstrand, A. 2015, *ApJL*, **814**, L2
 Fremling, C. 2022, *TNSR*, **167**, 1
 Galbany, L., Ashall, C., Höflich, P., et al. 2019, *A&A*, **630**, A76
 Garavini, G., Folatelli, G., Goobar, A., et al. 2004, *AJ*, **128**, 387
 Gehrels, N., Chincarini, G., Giommi, P., et al. 2004, *ApJ*, **611**, 1005
 Graham, M. J., Kulkarni, S. R., Bellm, E. C., et al. 2019, *PASP*, **131**, 078001
 Graham, M. L., Kumar, S., Hosseinzadeh, G., et al. 2017, *MNRAS*, **472**, 3437
 Guillochon, J., Dan, M., Ramirez-Ruiz, E., & Rosswog, S. 2010, *ApJL*, **709**, L64
 Harris, C. R., Millman, K. J., van der Walt, S. J., et al. 2020, *Natur*, **585**, 357
 HEASARC, 2014 HEASoft: Unified Release of FTOOLS and XANADU, Astrophysics Source Code Library, ascl:1408.004
 Hoefflich, P., Khokhlov, A. M., & Wheeler, J. C. 1995, *ApJ*, **444**, 831
 Howell, D. A., Sullivan, M., Nugent, P. E., et al. 2006, *Natur*, **443**, 308
 Hunter, J. D. 2007, *CSE*, **9**, 90
 Inserra, C., Sim, S. A., Wyrzykowski, L., et al. 2015, *ApJL*, **799**, L2
 Iwamoto, K., Brachwitz, F., Nomoto, K., et al. 1999, *ApJS*, **125**, 439
 Jacobson-Galán, W. V., Polin, A., Foley, R. J., et al. 2020, *ApJ*, **896**, 165
 Jerkstrand, A., Smartt, S. J., Sollerman, J., et al. 2015, *MNRAS*, **448**, 2482
 Jiang, J.-a., Doi, M., Maeda, K., et al. 2017, *Natur*, **550**, 80
 Johnson, B. D., Leja, J., Conroy, C., & Speagle, J. S. 2021, *ApJS*, **254**, 22
 Kasen, D. 2010, *ApJ*, **708**, 1025
 Kasen, D., Nugent, P., Wang, L., et al. 2003, *ApJ*, **593**, 788
 Kasen, D., Thomas, R. C., & Nugent, P. 2006, *ApJ*, **651**, 366
 Khokhlov, A. M. 1991, *A&A*, **245**, L25
 Kirby, E. N., Xie, J. L., Guo, R., et al. 2019, *ApJ*, **881**, 45
 Kromer, M., Sim, S. A., Fink, M., et al. 2010, *ApJ*, **719**, 1067
 Leibundgut, B., Kirshner, R. P., Phillips, M. M., et al. 1993, *AJ*, **105**, 301
 Li, W., Wang, X., Bulla, M., et al. 2021, *ApJ*, **906**, 99
 Lira, P. 1996, Master's thesis, Universidad de Chile
 Liu, C., Miller, A. A., Polin, A., et al. 2023a, *ApJ*, **946**, 83
 Liu, Z.-W., Röpke, F. K., & Han, Z. 2023b, *RAA*, **23**, 082001
 Livne, E. 1990, *ApJL*, **354**, L53
 Livne, E., & Arnett, D. 1995, *ApJ*, **452**, 62
 Maeda, K., Benetti, S., Stritzinger, M., et al. 2010a, *Natur*, **466**, 82
 Maeda, K., Taubenberger, S., Sollerman, J., et al. 2010b, *ApJ*, **708**, 1703
 Magee, M. R., & Maguire, K. 2020, *A&A*, **642**, A189
 Magee, M. R., Maguire, K., Kotak, R., & Sim, S. A. 2021, *MNRAS*, **502**, 3533
 Maguire, K., Sim, S. A., Shingles, L., et al. 2018, *MNRAS*, **477**, 3567
 Maguire, K., Sullivan, M., Pan, Y. C., et al. 2014, *MNRAS*, **444**, 3258
 Mahabal, A., Rebbapragada, U., Walters, R., et al. 2019, *PASP*, **131**, 038002
 Maoz, D., Mannucci, F., & Nelemans, G. 2014, *ARA&A*, **52**, 107

- Masci, F. J., Laher, R. R., Rusholme, B., et al. 2019, *PASP*, **131**, 018003
- Masci, F. J., Laher, R. R., Rusholme, B., et al. 2023, arXiv:2305.16279
- Matheson, T., Kirshner, R. P., Challis, P., et al. 2008, *AJ*, **135**, 1598
- Mazzali, P. A., Chugai, N., Turatto, M., et al. 1997, *MNRAS*, **284**, 151
- Mazzali, P. A., Sullivan, M., Filippenko, A. V., et al. 2015, *MNRAS*, **450**, 2631
- Mazzali, P. A., Sullivan, M., Hachinger, S., et al. 2014, *MNRAS*, **439**, 1959
- Miller, A. A., Yao, Y., Bulla, M., et al. 2020, *ApJ*, **902**, 47
- Miller, J., & Stone, R. 1994, The Kast Double Spectrograph, Lick Observatory Technical Report 66, Univ. California Observatories/Lick Observatory
- Motohara, K., Maeda, K., Gerardy, C. L., et al. 2006, *ApJL*, **652**, L101
- Newsome, M., Li, W., Burke, J., et al. 2022, *TNSCR*, **2167**, 1
- Ni, Y. Q., Moon, D.-S., Drout, M. R., et al. 2022, *NatAs*, **6**, 568
- Ni, Y. Q., Moon, D.-S., Drout, M. R., et al. 2023, *ApJ*, **946**, 7
- Noebauer, U. M., Kromer, M., Taubenberger, S., et al. 2017, *MNRAS*, **472**, 2787
- Nomoto, K. 1982a, *ApJ*, **253**, 798
- Nomoto, K. 1982b, *ApJ*, **257**, 780
- Nomoto, K. 1984, *ApJ*, **277**, 791
- Nomoto, K., Thielemann, F. K., & Yokoi, K. 1984, *ApJ*, **286**, 644
- Nugent, P. E., Sullivan, M., Cenko, S. B., et al. 2011, *Natur*, **480**, 344
- Oke, J. B., Cohen, J. G., Carr, M., et al. 1995, *PASP*, **107**, 375
- Oke, J. B., & Gunn, J. E. 1982, *PASP*, **94**, 586
- Oke, J. B., & Gunn, J. E. 1983, *ApJ*, **266**, 713
- Padilla Gonzalez, E., Howell, D. A., Burke, J., et al. 2023a, *ApJ*, **953**, 25
- Padilla Gonzalez, E., Howell, D. A., Terreran, G., et al. 2023b, arXiv:2308.06334
- Pakmor, R., Kromer, M., Taubenberger, S., & Springel, V. 2013, *ApJL*, **770**, L8
- Patat, F., Höflich, P., Baade, D., et al. 2012, *A&A*, **545**, A7
- Patterson, M. T., Bellm, E. C., Rusholme, B., et al. 2019, *PASP*, **131**, 018001
- Pereira, R., Thomas, R. C., Aldering, G., et al. 2013, *A&A*, **554**, A27
- Phillips, A. C., Miller, J., Cowley, D., & Wallace, V. 2006, *Proc. SPIE*, **6269**, 62691O
- Phillips, M. M., Lira, P., Suntzeff, N. B., et al. 1999, *AJ*, **118**, 1766
- Piascik, A. S., Steele, I. A., Bates, S. D., et al. 2014, *Proc. SPIE*, **9147**, 91478H
- Piro, A. L., & Morozova, V. S. 2016, *ApJ*, **826**, 96
- Piro, A. L., & Nakar, E. 2013, *ApJ*, **769**, 67
- Polin, A., Nugent, P., & Kasen, D. 2019, *ApJ*, **873**, 84
- Prochaska, J. X., Hennawi, J., Cooke, R., et al. 2020, pypeit/PypeIt: Release v1.0.0, Zenodo, doi:10.5281/zenodo.3743493
- Prochaska, J. X., Hennawi, J. F., Westfall, K. B., et al. 2020, *JOSS*, **5**, 2308
- Raskin, C., Kasen, D., Moll, R., Schwab, J., & Woosley, S. 2014, *ApJ*, **788**, 75
- Rigault, M., Neill, J. D., Blagorodnova, N., et al. 2019, *A&A*, **627**, A115
- Roming, P. W. A., Kennedy, T. E., Mason, K. O., et al. 2005, *SSRv*, **120**, 95
- Ruiter, A. J., Belczynski, K., Sim, S. A., et al. 2011, *MNRAS*, **417**, 408
- Ruiter, A. J., Belczynski, K., Sim, S. A., Seitenzahl, I. R., & Kwiatkowski, D. 2014, *MNRAS*, **440**, L101
- Salvatier, J., Wiecki, T. V., & Fonnesbeck, C. 2016, *PeerJ Computer Science*, **2**, e55
- Sanders, J. L., Belokurov, V., & Man, K. T. F. 2021, *MNRAS*, **506**, 4321
- Schlafly, E. F., & Finkbeiner, D. P. 2011, *ApJ*, **737**, 103
- Schulze, S., Krühler, T., Leloudas, G., et al. 2018, *MNRAS*, **473**, 1258
- Schulze, S., Yaron, O., Sollerman, J., et al. 2021, *ApJS*, **255**, 29
- Seitenzahl, I. R., Ciaraldi-Schoolmann, F., Röpke, F. K., et al. 2013, *MNRAS*, **429**, 1156
- Shen, K. J., Blondin, S., Kasen, D., et al. 2021a, *ApJL*, **909**, L18
- Shen, K. J., Boos, S. J., Townsley, D. M., & Kasen, D. 2021b, *ApJ*, **922**, 68
- Shen, K. J., Boubert, D., Gänsicke, B. T., et al. 2018a, *ApJ*, **865**, 15
- Shen, K. J., Kasen, D., Miles, B. J., & Townsley, D. M. 2018b, *ApJ*, **854**, 52
- Shingles, L., Smith, K. W., Young, D. R., et al. 2021, *TNSAN*, **7**, 1
- Shingles, L. J., Flörs, A., Sim, S. A., et al. 2022, *MNRAS*, **512**, 6150
- Siebert, M. R., Dimitriadis, G., Polin, A., & Foley, R. J. 2020, *ApJL*, **900**, L27
- Silverman, J. M., Foley, R. J., Filippenko, A. V., et al. 2012, *MNRAS*, **425**, 1789
- Smith, K. W., Smartt, S. J., Young, D. R., et al. 2020, *PASP*, **132**, 085002
- Speagle, J. S. 2020, *MNRAS*, **493**, 3132
- Steele, I. A., Smith, R. J., Rees, P. C., et al. 2004, *Proc. SPIE*, **5489**, 679
- Tanikawa, A., Nomoto, K., & Nakasato, N. 2018, *ApJ*, **868**, 90
- Tanikawa, A., Nomoto, K., Nakasato, N., & Maeda, K. 2019, *ApJ*, **885**, 103
- Taubenberger, S. 2017, in *Handbook of Supernovae*, ed. A. W. Alsabti & P. Murdin (Berlin: Springer), 317
- Taubenberger, S., Benetti, S., Childress, M., et al. 2011, *MNRAS*, **412**, 2735
- Taubenberger, S., Floers, A., Vogl, C., et al. 2019, *MNRAS*, **488**, 5473
- Tody, D. 1986, *Proc. SPIE*, **627**, 733
- Tonry, J. L., Denneau, L., Heinze, A. N., et al. 2018, *PASP*, **130**, 064505
- Townsley, D. M., Miles, B. J., Shen, K. J., & Kasen, D. 2019, *ApJL*, **878**, L38
- van der Walt, S., Crellin-Quick, A., & Bloom, J. 2019, *JOSS*, **4**, 1247
- Wang, L., Baade, D., Höflich, P., et al. 2003, *ApJ*, **591**, 1110
- Wang, L., & Wheeler, J. C. 2008, *ARA&A*, **46**, 433
- Wilk, K. D., Hillier, D. J., & Dessart, L. 2020, *MNRAS*, **494**, 2221
- Woosley, S. E., Taam, R. E., & Weaver, T. A. 1986, *ApJ*, **301**, 601
- Woosley, S. E., & Weaver, T. A. 1994, *ApJ*, **423**, 371
- Yao, Y., Miller, A. A., Kulkarni, S. R., et al. 2019, *ApJ*, **886**, 152
- Yaron, O., & Gal-Yam, A. 2012, *PASP*, **124**, 668
- Zackay, B., Ofek, E. O., & Gal-Yam, A. 2016, *ApJ*, **830**, 27
- Zheng, W., Kelly, P. L., & Filippenko, A. V. 2018, *ApJ*, **858**, 104